ACS OMEGA

http://pubs.acs.org/journal/acsodf

Article

Interaction of 5-Fluorouracil on the Surfaces of Pristine and Functionalized $Ca_{12}O_{12}$ Nanocages: An Intuition from DFT

Goodness J. Ogunwale, Hitler Louis,* Tomsmith O. Unimuke, Gideon E. Mathias, Aniekan E. Owen, Henry O. Edet, Obieze C. Enudi, Esther O. Oluwasanmi, Adedapo S. Adeyinka,* and Mohsen Doust Mohammadi

Cite This: *ACS Omega* 2023, 8, 13551−13568

Read Online

ACCESS | Metrics & More | Article Recommendations | Supporting Information

ABSTRACT: The utilization of nanostructured materials for several biomedical applications has tremendously increased over the last few decades owing to their nanosizes, porosity, large surface area, sensitivity, and efficiency as drug delivery systems. Thus, the incorporation of functionalized and pristine nanostructures for cancer therapy offers substantial prospects to curb the persistent problems of ineffective drug administration and delivery to target sites. The potential of pristine ($Ca_{12}O_{12}$) and formyl (−CHO)- and amino ($-NH_2$)-functionalized ($Ca_{12}O_{12}$−CHO and $Ca_{12}O_{12}$−NH_2) derivatives as efficient nanocarriers for 5-fluorouracil (5FU) was studied at the B3LYP-GD3(BJ)/6-311++G(d,p) theoretical level in two electronic media (gas and solvent). To effectively account for all adsorption interactions of the drug on the investigated surfaces, electronic studies as well as topological analysis based on the quantum theory of atoms in molecules (QTAIM) and noncovalent interactions were exhaustively utilized. Interestingly, the obtained results divulged that the 5FU drug interacted favorably with both $Ca_{12}O_{12}$ and its functionalized derivatives. The adsorption energies of pristine and functionalized nanostructures were calculated to be −133.4, −96.9, and −175.6 kcal/mol, respectively, for $Ca_{12}O_{12}$, $Ca_{12}O_{12}$−CHO, and $Ca_{12}O_{12}$−NH2. Also, both topological analysis and NBO stabilization analysis revealed the presence of interactions among O_3−H_{32}, O_{27}−C_{24}, O_{10}−C_{27}, and N_{24}−H_{32} atoms of the drug and the surface. However, 5FU@$Ca_{12}O_{12}$−CHO molecules portrayed the least adsorption energy due to considerable destabilization of the molecular complex as revealed by the computed deformation energy. Therefore, 5FU@$Ca_{12}O_{12}$ and 5FU@$Ca_{12}O_{12}$−NH_2 acted as better nanovehicles for 5FU.

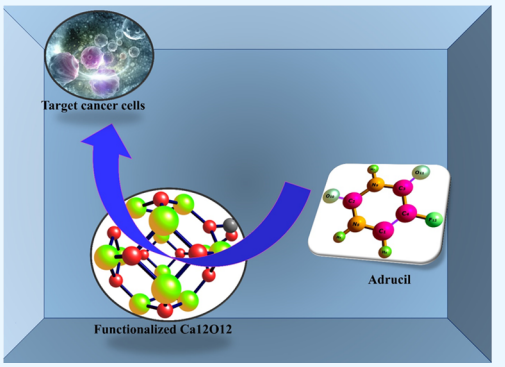

1. INTRODUCTION

According to a recent report by the World Health Organization (WHO), nearly ten million people lost their lives to cancer in 2020, making it the second leading cause of death worldwide.[1,2] 5-Fluorouracil (5FU), with the brand name Adrucil, is an effective anticancer drug commonly used for the chemotherapeutic treatment of colorectal, esophageal, stomach, pancreatic, breast, and cervical cancers.[3] The 5FU drug, which is administered orally, activates by a mechanism involving its incorporation into the phosphates of the ribonucleic acid (RNA) and deoxyribonucleic acid (DNA) such that it inhibits nucleoside metabolism and DNA replication. Nevertheless, the drug's administration possesses a short biological half-life, low selectivity, and toxic side effects on the bone marrow.[3−5] This is a leading challenge in chemotherapy, that is, the targeted delivery of anticancer drugs. Drug delivery systems have been challenged by factors like hepatotoxicity, immunogenicity, bioavailability, and safety.[5−7] However, in recent years, efforts have been made to overcome these challenges. Liposomes,[8,9] polymers,[10,11] dendrimers,[12,13] and nanostructures[14−16] have been explored as drug delivery systems in cancer treatment.

Nanostructures, first discovered in 1985 by Kroto et al.,[17] have drawn scientific interest in their potential applications as drug nanocarriers. Due to their unique structures and properties such as high biocompatibility, low toxicity, and chemical inertness,[18,19] numerous carbon or non-carbon inorganic nanostructures such as nanosheets,[20,21] nanotubes,[22,23] or fullerene-like nanocages[24,25] have been investigated for their applications in medicine,[26,27] quantum computing,[28,29] optics,[30,31] gas sensor detection,[32,33] drug delivery,[34,35] and electronics.[36,37] Nanostructures enhance drug solubility, reduce toxicity and side effects of drugs, and in situ drug release to the desired target site (tumor

Received: June 10, 2022
Accepted: January 11, 2023
Published: April 3, 2023

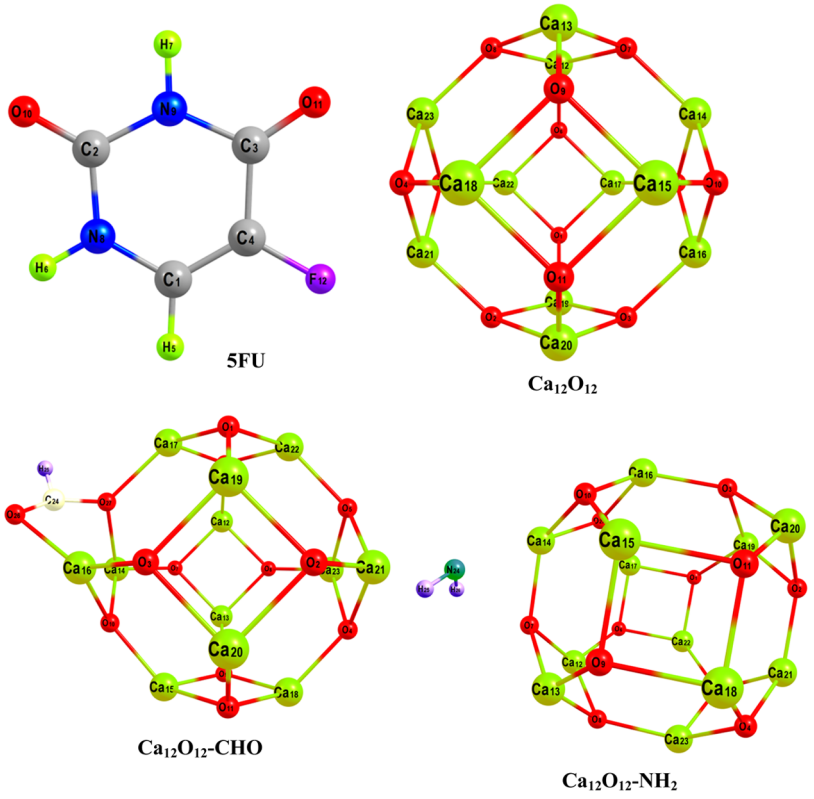

Figure 1. Optimized geometry of 5-fluorouracil (5FU) and the studied nanocages.

environment).[34,35,38] Carbon nanotube is one of the most popular nanocarrier systems for drug delivery in pharmaceutics and medicine. But carbon nanotubes, as carriers of anticancer drugs, have a problem of low solubility and high toxicity.[22,39] Consequently, the application of inorganic non-carbon nanocages has been of great interest. It was reported that inorganic fullerene-like nanocages, formed from group II−VI elements of the periodic table, with the structural formula $X_{12}Y_{12}$ possess the most stable structures.[24,40−42] However, nanocages formed from metal oxides such as calcium oxide ($Ca_{12}O_{12}$) have been found quite useful due to the ionic nature of the Ca−O bond, stability, and minimum chemical reactivity.[32,43] Generally, to enhance the drug delivery properties of nanotubes and nanocages, the introduction of dopant atoms or chemical functionalization has been employed.[44] Functionalizing nanocages with functional groups containing oxygen, nitrogen, carbon, and hydrogen atoms improve drug solubility in the solvent phase through electrostatic, $\pi \rightarrow \pi$, or hydrogen bonding interactions. Omidi et al.[45] reported that Sc doping greatly enhanced the conductance properties of $Be_{12}O_{12}$, $Mg_{12}O_{12}$, and $Ca_{12}O_{12}$. Hussain et al.[46] reported that zinc-decorated inorganic $Mg_{12}O_{12}$ nanoclusters were very efficient as gas sensors for $COCl_2$ adsorption. Assessment of the adsorption mechanism of the flutamide anticancer drug on the functionalized single-walled carbon nanotube surface by Kamel et al.[47] indicated that the drug was strongly adsorbed on the functionalized carbon nanotube when compared to the pristine carbon nanotube. In more recent work, Sajid et al. (2022)[48] reported that the adsorption of some studied small gaseous molecules (N_2O, NO_2, NO, H_2S, SO_2, and SO_3) onto three selected nanocages followed the trend $Ca_{12}O_{12} > Mg_{12}O_{12} > Be_{12}O_{12}$. Similarly, Vatanparast and Shariatinia[49] investigated the interaction of 5-fluorouracil anticancer drug molecules and undoped/doped graphene quantum dots (GQDs). They reported that doping of GDQs significantly enhanced the adsorption of 5FU on the surface. Bagheri and his co-workers[50] reported that pristine phagraphene was inappropriate for Adrucil drug delivery, but when doped with Al, Si, or B atoms, doped phagraphene was appropriate for drug delivery.

Based on these reports, the efficacy of calcium oxide nanoclusters as well as their functionalized derivatives (formyl (−CHO)- and amino ($-NH_2$)-functionalized), which are designated as $Ca_{12}O_{12}$−CHO and $Ca_{12}O_{12}$−NH_2, respectively, is investigated herein as potential drug delivery vehicles for the 5-fluorouracil (5FU) anticancer drug (see Figure 1). To effectively appraise the efficacy of the considered nanostructured material, the density functional theory approach based on first principles computation is deployed to assess the extent and nature of the interaction of the drug molecule with the studied nanoclusters. Molecular electronic properties of the systems are also considered to gain considerable insight into the electronic behavior of the nanoclusters prior to and after adsorption. Finally, topological analysis based on the quantum theory of atoms in molecules and noncovalent interactions as well as electron localization function is employed to reveal and quantify the nature and strength of the interaction between the adsorbed drug and the nanostructured surfaces.

2. COMPUTATIONAL DETAILS

All geometry optimization of the studied compounds was performed using Gaussian 16 software version 3.2[51] within the *meta*-generalized gradient approximation (*Meta*-GGA) framework. The exchange−correlation functional of Becke−3−Lee−Yang−Parr (B3LYP) coupled with the third version of Grimme's atomic pair-wise dispersion correction (D3)

https://doi.org/10.1021/acsomega.2c03635
ACS Omega 2023, 8, 13551−13568

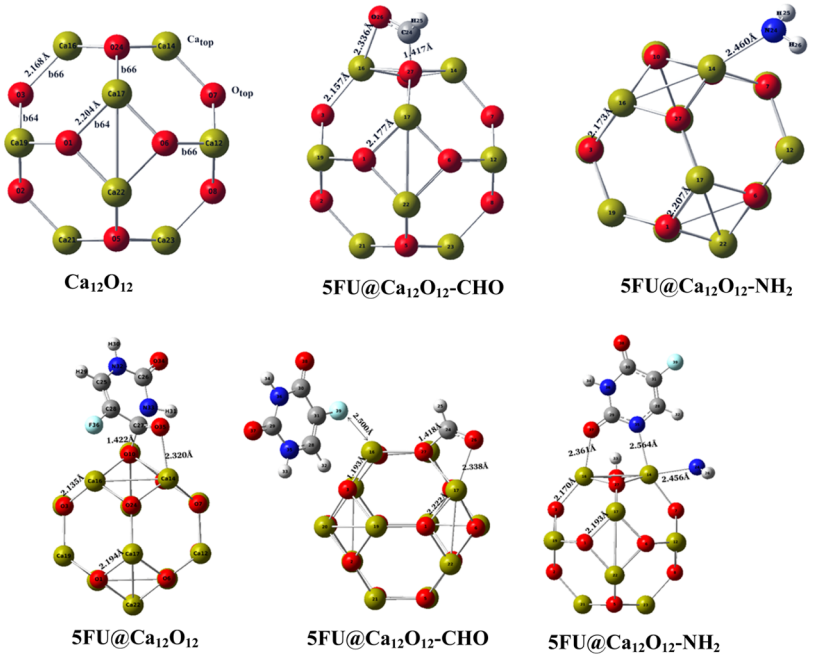

Figure 2. Bond length and geometry of pristine $Ca_{12}O_{12}$ and its functionalized derivatives, as well as the adsorbed nanocages.

combined with Becke–Johnson (BJ) damping (B3LYP-GD3BJ), which gives an account of the long-range dispersion interactions, empirically was utilized accordingly for geometry optimization.[52] In all cases, the geometries were optimized using Pople's triple zeta split valence basis set (6-311++G(d,p)) and subjected to a basis set superposition error (BSSE)-corrected single point energy calculation using the same basis set.[53] To ensure accuracies of computations, frequency calculations were performed at the same level of theory (B3LYP-GD3 (BJ)/6-311++G(d,p)) to ascertain the absolute correspondence of the optimized geometry to local minima on the potential energy surface. For computations in solution, the conductor-like polarizable continuum solvation model (CPCM)[54] was adopted implicitly with water as a solvent to account for the solvation effect during computations of adsorption energies. All computations in solution were achieved at the same theoretical level as the gas-phase optimization. All calculations were performed to meet the normal convergence criteria in the Gaussian 16 code, and the convergence criteria adopted for the SCF calculations were set to tight SCF to reduce numerical noises. The adsorption energies (E_{ad}) of 5FU on the surfaces of the nanomaterials were calculated using the following eq 1

$$E_{ad} = E_{5FU/nanocage} - E_{5FU} - E_{nanocage} + E_{(BSSE)} + ZPE \quad (1)$$

where $E_{5\text{-}FU/nanocage}$ designates the total energy of the complexes after the adsorption of the 5FU drug on the nanocages, E_{5FU} represents the energy of the 5FU drug molecule before interaction, and $E_{nanocage}$ designates the energy of the isolated nanocages before interaction, while E_{BSSE} tackles the induced error in energy calculations due to basis set incompleteness; the BSSE was conducted by running a single point energy calculation on the B3LYP-GD3BJ optimized geometry with the inclusion of counterpoise correction. To obtain detailed insight into the nature of the interatomic interactions, topological analysis based on the quantum theory of atoms in a molecule as well as noncovalent interaction analysis was conducted on the B3LYP-GD3(BJ)/6-311++G(d,p) optimized geometry using Multiwfn software version 3.7.[55] For visualization and renderings of isosurface maps, virtual molecular dynamics (VMD) software[56] was utilized. The natural bond orbital (NBO) analysis was conducted at the same level of theory as the optimized geometry with the help of the NBO 7.0 program embedded in the Gaussian 16 program.[51] Molecular electrostatic potential (MEP) isosurface maps and density of states (DOS) plots were generated based on the density functional theory (DFT)/B3LYP-GD3BJ/6-311++G(d,p) optimized geometry, and the graphical renderings were obtained using GaussView 6.0.16 and Multiwfn 3.7 software, respectively. Figure 1 shows the optimized geometry of 5FU and the studied nanocages.

3. RESULTS AND DISCUSSION

3.1. Geometrical Structural Analysis. To determine the orientation with the best adsorption configuration and stability, the interactions of 5FU with $Ca_{12}O_{12}$ and formyl-functionalized ($Ca_{12}O_{12}$–CHO) and amino-functionalized ($Ca_{12}O_{12}$–NH_2) derivatives (Figure 1) was first considered at different orientations. The studied nanocages together with bond distances prior to and after adsorption are depicted in Figure 2. From Figure 2, it is pertinent that the pristine $Ca_{12}O_{12}$ nanocage exhibit tetrahedral (T_h) symmetry and mainly contains the b_{66} and b_{64} bonds. The b_{66} (Ca_{16}–O_3) bond is the bond between two hexagonal rings, while b_{64} (Ca_{17}–O_1) is the bond between tetragonal and hexagonal rings. However, the b_{66} and b_{64} bond lengths for pristine $Ca_{12}O_{12}$ were calculated to be 2.168 and 2.204 Å, respectively. These bond lengths are found to be consistent with previous computational results.[64−69] As presented in Figure 2, for the adsorbed nanocages, the calculations showed that the 5FU drug preferred to interact via the O, N, F, and C atoms. The 5FU drug interacted with the nanocages by forming weak bonds at different positions. In $Ca_{12}O_{12}$, the drug is observed to interact with the surface at calculated distances of 1.42 Å between C_{27} and O_{10} and 2.32 Å between O_{35} and Ca_{14}. Similarly, the

https://doi.org/10.1021/acsomega.2c03635
ACS Omega 2023, 8, 13551−13568

fluorine atom (F_{38}) of 5FU is observed to be inclined toward the $Ca_{12}O_{12}$−CHO nanocage, thereby interacting with the Ca_{16} atom at 2.30 Å, while in $Ca_{12}O_{12}$−NH_2, the drug preferred to interact via N_{35} and O_{37} with Ca_{14} and Ca_{16} of the surface, respectively. Despite the stable nature of these interactions with the drug, considerable deformations in bond geometry induced by adsorption are observable. The bond length between the tetragonal ring (Ca_{17}—O_1) was calculated to be 2.204 Å, while the bond length between hexagonal rings (Ca_{16}—O_3) was found to be 2.168 Å in the case of the pristine $Ca_{12}O_{12}$ nanocage. Both bond lengths were observed to increase in slight proportions as a result of the adsorption of 5FU. A slight increase from 2.170 to 2.192 Å was seen in the $Ca_{12}O_{12}$−NH_2 system, whereas in the case of the $Ca_{12}O_{12}$ system, a decrease in bond length of Ca_{16}—O_{12} was observed with a calculated difference of 0.033 Å. This elongation in bonds is probably the consequence of charge transfer between the adsorbate and the adsorbent. Table 2 shows the total charge transferred between the adsorbate and the adsorbent; the results express that each surface assumes a negative charge after the adsorption of 5FU, thus affirming the presence of charge transfer interactions with the surfaces. Further, no visible variation in the bond length of 5FU drug molecules in most of the studied complexes before and after adsorption was observed, meaning the drug maintained its geometry during the adsorption process. These results indicate that interactions between the 5FU drug and the nanocages result in no depreciation of the drug molecule. However, deformation energies are computed in a subsequent section. Table S1 shows the detailed geometrical properties of the drug and surfaces, while Table 1 shows the selected bond lengths of the complexes.

Table 1. Selected Bond Lengths for All Studied Complexes Calculated at the DFT/B3LYP-GD3BJ/6-311++G(d,p) Level of Theory

		bond length (Å)	
system	bond label	before adsorption	after adsorption
$Ca_{12}O_{12}$	Ca_{16}−O_3	2.17	2.14
	Ca_{17}−O_1	2.20	2.19
	C_{27}−O_{10}		1.42
	C_{27}−O_{35}	1.31	1.31
	Ca_{14}−O_{35}		2.32
$Ca_{12}O_{12}$−CHO	Ca_{16}−O_3	2.16	1.19
	Ca_{17}−O_1	2.18	2.22
	C_{16}−O_{26}	2.34	2.34
	O_{27}−C_{24}	1.42	1.45
	Ca_{16}−F_{39}	2.49	2.50
$Ca_{12}O_{12}$−NH_2	Ca_{16}−O_3	2.17	2.17
	Ca_{17}−O_1	2.21	2.19
	C_{14}−N_{24}	2.46	2.46
	Ca_{16}−O_{37}	2.37	2.36
	Ca_{16}−N_{35}	2.55	2.56

3.2. Adsorption Study. To appraise the level of interaction between the drug molecule with the studied adsorbent surfaces, the adsorption energies of the drug with each surface are calculated separately. The interaction energies have been calculated based on the optimized geometries at the B3LYP-GD3 (BJ)/6-311++G(d,p) level. To further account for the solvent effect on the interaction energy, adsorption energies were equally calculated by conducting frequency calculations in solvent (water) at the same level of theory as the optimized geometry. The values of the computed adsorption energies (E_{ad}) are reported in Table 2. It is pertinent from the most stable geometry of the drug and the surface that the interaction between the adsorbate and the adsorbent is due to the presence of electronegative oxygen atoms on the nanocluster surface, which are attracted to the electropositive hydrogen atoms of the drug molecule. Also, the electronegative atoms in the drug molecule play the same role of facilitating the interaction with electropositive Ca atoms on the surface. The adsorption energies of the most stable orientation of 5FU on the surfaces of $Ca_{12}O_{12}$, $Ca_{12}O_{12}$−CHO, and $Ca_{12}O_{12}$−NH_2 are found to be within the range from −97.5 to −175.6 kcal/mol, and the BSSE-corrected energies are also observed in the same range, with only a slight decrease in the computed energy. The BSSE-corrected energies are −133.4, −96.9, and −175.5 kcal/mol, respectively, for $Ca_{12}O_{12}$, $Ca_{12}O_{12}$−CHO, and $Ca_{12}O_{12}$−NH_2 surfaces. Due to the disruption of the symmetries of the nanocages as a result of functionalization with formyl and amino groups, the resulting special effects account for the observed decrease/increase in the adsorption energies of $Ca_{12}O_{12}$−CHO and $Ca_{12}O_{12}$−NH_2, respectively. The adsorption energy in the case of $Ca_{12}O_{12}$−CHO slightly decreases from −136.8 kcal/mol in $Ca_{12}O_{12}$ to −97.5 kcal/mol, whereas the adsorption energy increases in the case of $Ca_{12}O_{12}$−NH_2 (amino-functionalized derivative) from −136.8 kcal/mol as observed in $Ca_{12}O_{12}$ to −175.5 kcal/mol. Several literature reports affirm that the more negative adsorption energies tend to be, the better the interactions of the adsorbate on the surface of the adsorbent. Thus, by comparing the adsorption energies of the functionalized ($Ca_{12}O_{12}$−CHO and $Ca_{12}O_{12}$−NH_2) and unfunctionalized nanocages ($Ca_{12}O_{12}$), it is ostensible that the functionalized surface ($Ca_{12}O_{12}$−NH_2) that has more negative adsorption energy acted as a better nanovehicle for 5FU. Based on the computed adsorption energies, which are within the range from −97.5 to −175.6 kcal/mol, the mechanism of adsorption can therefore be classified as chemisorption, and the negative values of the adsorption enthalpies is an indication of the stable adsorption configuration of 5FU with the respective surfaces. For a surface to act as a good nanovehicle, the adsorption energy should not be too high and too weak, to enable the ease of desorption from the surface. Based on this reality, the suitability of $Ca_{12}O_{12}$ and $Ca_{12}O_{12}$−NH_2 is further confirmed. To accurately account for the stability of interaction, the deformation energies of 5FU with each surface are further calculated, as presented in Table 2. The results obviously disclosed that $Ca_{12}O_{12}$ and $Ca_{12}O_{12}$−NH_2 with negative adsorption enthalpies are less deformed than $Ca_{12}O_{12}$−CHO. $Ca_{12}O_{12}$−CHO experienced the greatest deformation amounting to −1.8 kcal/mol, thus divulging that the compatibility of its surface with 5FU is less than that of other derivatives. The strong deformation energy in $Ca_{12}O_{12}$−CHO shows that F5U forms a strong bond with the surface, and therefore, the ease of desorption will not be feasible. More so, during the adsorption process, a significant charge was observed to be transferred from the drug to the surface. The charge transfer quantified by the NBO charge is also given in Table 2. The results disclosed that the negative charge was transferred from the adsorbate to the adsorbent in all cases of $Ca_{12}O_{12}$, $Ca_{12}O_{12}$−CHO, and $Ca_{12}O_{12}$−NH_2 adsorption. This charge transfer is prompted by the electronegativity difference between the adsorbate and the adsorbent, and the results are in tandem with other computed

https://doi.org/10.1021/acsomega.2c03635
ACS Omega 2023, 8, 13551−13568

Table 2. Adsorption Energies (E_{ad}) (kcal/mol), Deformation Energy (E_{def}), NBO Charge ($Q(\acute{e})$), and Zero-Point Vibrational Energy of the Studied Systems Calculated at the DFT/B3LYP-GD3BJ/6-311++G (d,p) Level of Theory Set in Gas and Water Phases

systems	E_{ads}(kcal/mol) water	E_{ad}(kcal/mol) gas	BSSE corrected (kcal/mol)	ZPE (kcal/mol)	E_{def}	E_{sol}	$Q(\acute{e})$
$Ca_{12}O_{12}$	−133.4	−136.8	−133.4	79.28	−62.7	−140.2	−0.9
$Ca_{12}O_{12}$−CHO	−96.9	−97.5	−96.9	90.19	−1.8	−143.8	−0.04
$Ca_{12}O_{12}$−NH_2	−175.5	−175.6	−175.5	92.76	−42	−138.1	−0.5

Table 3. Reported Adsorption Energies (E_{ad}) of Various Adsorption Interactions Involving Both $Ca_{12}O_{12}$ and the 5FU Drug with Other Studied Nanosurfaces

system	E_{ad} in kcal/mol	method	ref
Previous Works on the Adsorption of Different Adsorbents on $Ca_{12}O_{12}$ Nanocages			
AlP/$Ca_{12}O_{12}$ (A) and AlP/$Ca_{12}O_{12}$ (B)	−11.9 and 4.2	B3LYP-D3/6-31G*	61
N_2O/$Ca_{12}O_{12}$, NO_2/$Ca_{12}O_{12}$, and NO/$Ca_{12}O_{12}$	−11.8, −46.5, and −26.5	B3LYP-D3/6-31G(d)	46
H_2S/$Ca_{12}O_{12}$, SO_2/$Ca_{12}O_{12}$, and SO_3/$Ca_{12}O_{12}$	−50.3, −78.6, and −123.6		
mustard/$Ca_{12}O_{12}$ (A) and mustard/$Ca_{12}O_{12}$ (B)	−11.0 and −30.9	B3LYP-D3/6-31G*	62
H_2O/$Ca_{12}O_{12}$ and H_2S/$Ca_{12}O_{12}$	−23.8 and −42.2	MPW1PW91/6-311G(d,p)	63
H_2O/$Ca_{12}O_{12}$ and H_2S/$Ca_{12}O_{12}$	−24.7 and −42.6	wB97XD/6-311G(d,p)	
Previous Works on the Adsorption of the 5FU Drug on Other Various Nanosurfaces			
5FU/$Zn_{12}O_{12}$, 5FU/Al-doped $Zn_{12}O_{12}$, 5FU/Fe-doped $Zn_{12}O_{12}$, 5FU/Ga-doped $Zn_{12}O_{12}$, and 5FU/Mg-doped $Zn_{12}O_{12}$	−18.4, −24.4, −30.9, −32.1, and −42.8	B3LYP/LANL2DZ	64
5FU/BNNT, 5FU/$B_{12}N_{12}$, and 5FU/PBNP	−15.1, −27.0, and −19.1	GGA-PBE	65
adrucil/phagraphene, adrucil/B-doped, adrucil/Al-doped, and adrucil/Si-doped	−2.6, −6.8, −41.8, and −14.0	B3LYP-D3/6-31G*	50
5FU/ZnO and 5FU/ZnO	−19.4 and −25.8	B3LYP-D3/LANL2DZ	66

Table 4. Calculated Solvation Energies of the Studied System

systems						
5FU	$Ca_{12}O_{12}$	$Ca_{12}O_{12}$−CHO	$Ca_{12}O_{12}$−NH_2	5FU@$Ca_{12}O_{12}$	5FU@$Ca_{12}O_{12}$−CHO	5FU@$Ca_{12}O_{12}$−NH_2
Energies in kcal/mol						
−24.04	−222.76	−230.95	−222.20	−140.153	−143.79	−138.08

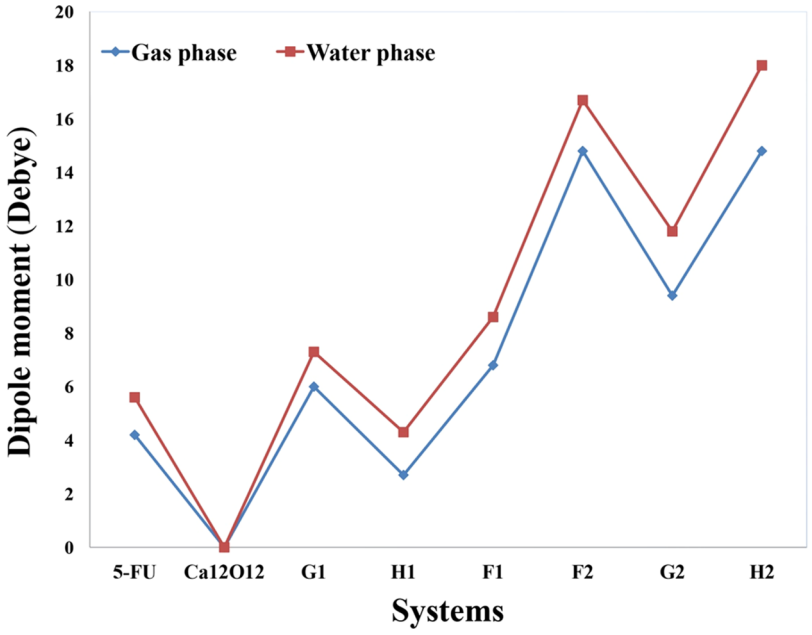

Figure 3. Dipole moments (Debye) of all of the studied systems at the DFT/B3LYP-GD3BJ/6-311++G(d,p) level of computations.

results. Further, this result is comparable with other reported literature studies. Ahsan et al. investigated the therapeutic potential of amino-functionalized cyclodextrin (C_2N) as a drug delivery system for fluorouracil and nitrosourea for cancer treatment. The computed adsorption energies for both fluorouracil and nitrosourea were observed to be −26.3 and −26.4 kcal/mol, respectively. Similarly, de Oliveira et al. studied the interaction of 5FU on BNNT, BN, and PBNP nanostructured materials. The calculated interaction energies for all cases were found to be −15.1, −27.0, and −19.1 kcal/mol, respectively.[57,64] Also, Soltani et al. calculated the adsorption energy for the interaction of 5-fluorouracil on the

https://doi.org/10.1021/acsomega.2c03635
ACS Omega 2023, 8, 13551−13568

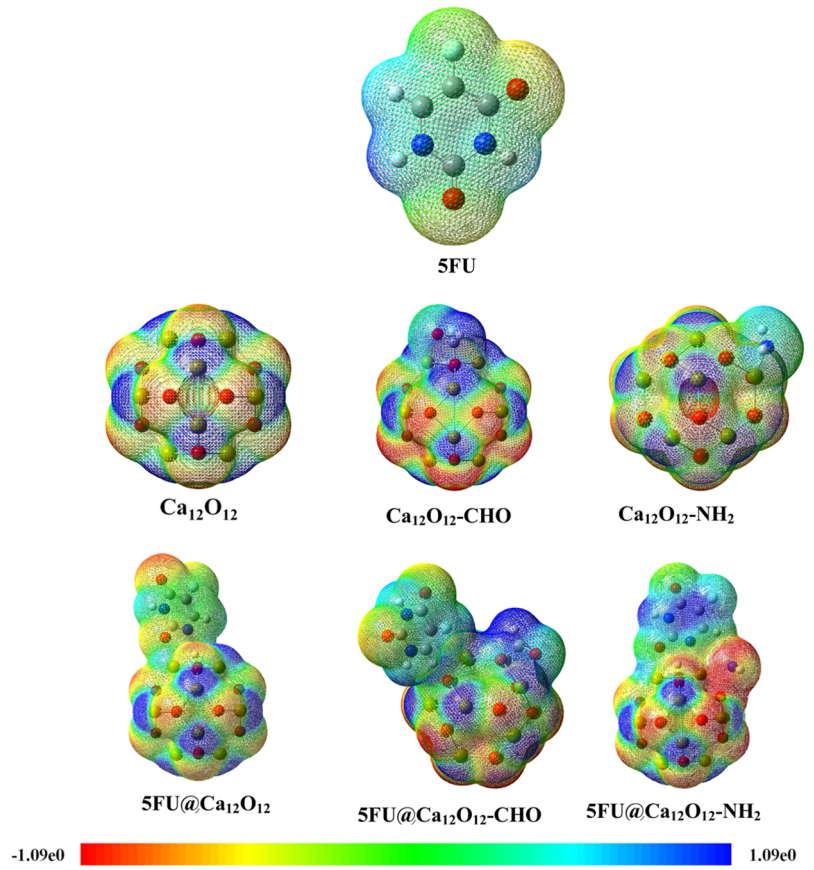

Figure 4. Molecular electrostatic potential maps showing electron density isosurface for all systems. The color range is in atomic unit (a.u). Blue and light blue: positive region, green: zero region, and yellow and red: negative regions.

surfaces of pure and doped boron nitride nanotubes to be −40.27, −32.95, and −20.95 kcal/mol for Ge-, Ga-, and Al-doped BN, respectively.[58] Moreover, the adsorption behavior of 5-fluorouracil on B_{40}, $B_{39}M$, and $M@B_{40}$ (M = Mg, Al, Si, Mn, Cu, Zn) was investigated by Zhang et al. The calculated adsorption energies for the respective systems were in the range from −11.15 to −29.75 kcal/mol, while the interaction energy was found to be in the range from −13.65 to −35.44 kcal/mol.[59] Other reported works on related surfaces are presented in Table 3. This result is also in line with the experimental assessment of the utilization of calcium oxide nanoparticles as drug delivery systems as reported by ref 60. Their findings clearly demonstrate that calcium oxide nanoparticles acted better as delivery systems in vitro when functionalized with suitable groups.

3.3. Solvation Energy. To further investigate the degree and influence of solvation on the adsorption enthalpies of the studied systems, the solvation enthalpy for the studied systems is computed using eq 3, and the theoretical calculations were performed implicitly using the polarizable continuum solvation model and water as the solvent. The obtained results of the solvation enthalpy parameter are tabulated in Table 4.

$$E_{sol} = E_{T.sol} - E_{gas} \quad (2)$$

where $E_{T.sol}$ and E_{gas} are the total energies of the systems in the water and gas phases, respectively.

Based on the computed solvation energies, the energies of the interacted nanoclusters decreased considerably upon the adsorption of 5FU. The negative solvation enthalpies as obtained are indicative of a spontaneous solvation process and therefore suggest that the studied systems are relatively soluble in an aqueous environment. Also, the possibility of dispersal in a living system is affirmed based on this premise.

3.4. Dipole Moment and Molecular Electrostatic Potential (MEP). The nature of molecular dipole moment efficiently allows the holistic insight into the charge separation within a system or complex to be appraised. Molecular dipole moments also permit the strength of interactions within complexes to be predicted.[67,68] The calculated dipole moments of the respective systems were obtained from the DFT/B3LYP-GD3 (BJ) optimized geometry in gas and water. The results are presented in Table S5 of the Supporting Information, while the plot is depicted in Figure 3. The results disclosed that pristine $Ca_{12}O_{12}$ is nonpolar with a dipole moment of zero-dimensional (0D) in all phases, which stems from the absence of charge separation and the centrosymmetric nature of the $Ca_{12}O_{12}$ nanocluster such that there is a nullifying resultant dipole moment from the equal positively charged Ca atoms and negatively charged O atoms. However, the functionalized nanocages are polar in nature; hence, functionalization of pristine $Ca_{12}O_{12}$ significantly resulted in an increase in dipole moment from 0D to 6.096 D as observed in $Ca_{12}O_{12}$−CHO and 2.719 D in the case of $Ca_{12}O_{12}$−NH_2. Also, the 5FU drug is observed to exhibit polarity with a corresponding dipole moment of 4.215 D in the gas phase. Interestingly, it was observed that after the adsorption of the 5FU drug, the dipole moment for all complexes significantly increased, as clearly depicted in Table S2 and Figure 3. As such, the dipole moments in $Ca_{12}O_{12}$, $Ca_{12}O_{12}$−CHO, and $Ca_{12}O_{12}$−NH_2 complexes are 14.859, 9.482, and 14.869 D,

https://doi.org/10.1021/acsomega.2c03635
ACS Omega 2023, 8, 13551−13568

Table 5. Second-Order Perturbation Energies ($E^{(2)}$) (kcal/mol) of the Studied Complexes Calculated at the DFT/B3LYP-GD3BJ/6-311++G (d,p) Basis Level[a]

systems	donor (i)	ED (e)	acceptor (j)	ED (e)	$E^{(2)}$	$E_{(j)} - E_{(i)}$ (a.u)	$F_{(i,j)}$ (a.u)
$Ca_{12}O_{12}$	$\sigma O_{10}-C_{27}$	1.99078	$\sigma^*C_5-C_{28}$	1.98356	1.08	1.46	0.036
	$C_{27}-O_{35}$	1.99242	$Lp^*(1)Ca_{14}$	0.01930	1.03	1.16	0.031
	$LP(1)O_{34}$	1.96676	$LP^*(1)Ca_{16}$	0.07878	7.28	0.98	0.076
	$LP(1)N_{32}$	1.88460	$\sigma^*O_{10}-H_{30}$	1.99688	14.55	0.83	0.100
$Ca_{12}O_{12}-CHO$	$LP(2)O_6$	0.97340	LP^*Ca_{12}	0.03200	4.67	0.56	0.046
	$LP(3)O_6$	0.96867	LP^*Ca_{22}	0.03200	2.27	0.43	0.028
	$LP(3)O_{27}$	0.91291	$\pi^*C_{24}-O_{26}$	0.99360	18.06	0.33	0.098
	$\pi C_{28}-C_{31}$	0.92436	$\pi^*C_{30}-O_{38}$	0.99156	11.82	0.32	0.080
$Ca_{12}O_{12}-NH_2$	$LP^*(1)Ca_{14}$	1.00000	$\sigma^*C_{29}-O_{37}$	0.01125	0.03	0.20	0.012
	$LP^*(1)Ca_{14}$	1.00000	$\sigma^*C_{28}-N_{35}$	0.00689	0.18	0.20	0.012
	$LP^*(1)Ca_{14}$	1.00000	$\sigma^*C_{29}-O_{37}$	0.01125	0.3	0.20	0.012
	$LP^*(1)Ca_{14}$	1.00000	$\sigma^*C_{29}-N_{35}$	0.02472	0.18	0.17	0.025
	$\pi^*C_{29}-N_{35}$	0.24193	$\pi^*C_{28}-C_{31}$	0.01440	21.30	0.04	0.062

[a] $E_{(j)} - E_{(i)}$ designates the difference in energy term for each donor and acceptor interacting orbital, $F_{(i,j)}$ represents the off-diagonal Fock matrix, and ED is the occupancy (electrons transferred during interaction).

respectively, at the DFT/B3LYP-GD3 (BJ) theoretical level in the gas phase, resulting from considerable charge separation between the 5FU drug and the nanocages. Nevertheless, the large dipole moments observed in $Ca_{12}O_{12}$ and $Ca_{12}O_{12}-NH_2$ complexes could result from higher charge separation. However, an increase in the dipole moment indicates a corresponding increase in the polarity and solubility of the polar media (water).[69] It was further observed that the calculated dipole moment values obtained with the ωB97XD method were slightly higher than those obtained with the B3LYP-GD3(BJ) method, and the dipole moments of the complexes increased significantly in water media compared to the gas phase, suggesting a corresponding increase in the solubility of the isolated systems (see Figure 3)

The molecular electrostatic potential (MEP) map is an important tool for studying the reactivity of a molecule because it gives insight into the active sites for electrophilic and nucleophilic attacks in the molecule through electron density distributions.[70] The three-dimensional MEP contour maps for the 5FU drug and other studied systems are presented in Figure 4. The MEP map can be interpreted using the red-yellow-green-blue color scale and different electrostatic potential values. Similarly, blue or light blue coloration at any point on the map indicates a positive electrostatic potential (electron-deficient) region and is thus susceptible to nucleophilic attack; green color corresponds to zero potential regions; red- or yellow-colored regions have negative electrostatic potential (electron-rich) and are favorable for electrophilic attack.[71,72] From Figure 4, it can be observed that negative potential regions are found on oxygen atoms (yellow color), while positive potential regions are located on hydrogen atoms (blue color) in the 5FU drug. However, pristine $Ca_{12}O_{12}$ has a symmetrical potential, which results from the centrosymmetrical nature of $Ca_{12}O_{12}$, such that the Ca atoms have positive electrostatic potentials (blue color), and the O atoms have a negative electrostatic potential (yellow color). Functionalization of the pristine $Ca_{12}O_{12}$ nanocage strengthened its positive electrostatic potential, as evident from the extra blue colors observed in both $Ca_{12}O_{12}-CHO$ and $Ca_{12}O_{12}-NH_2$ nanocages. Furthermore, the MEP maps for the complexes $Ca_{12}O_{12}$, $Ca_{12}O_{12}-CHO$, and $Ca_{12}O_{12}-NH_2$ disclosed that the O atoms in 5FU bonded toward the electropositive Ca atoms from the nanocages, while H atoms tended toward the electronegative O atoms from the nanocages. These results provide insight into active sites for interactions between the 5FU drug and the nanocages as observed in the complexes and thus agree with the charge transfer pattern obtained from the calculated dipole moments. Thus, the results suggest that the modeled complexes exhibit significant potential as candidates for drug delivery.

3.5. Natural Bond Orbital (NBO) Analysis. Natural bond orbital analysis, developed by Weinhold et al.,[73] is an important technique that unravels information on the electron distribution within the intermolecular bonds between atomic species and gives insight into the charge transfer pattern in the studied systems. However, NBO analysis provides adequate knowledge on the bonding orbital type, occupancy level, and also the nature of interactions present in the valence space between the virtual and occupied Lewis orbitals.[74,75] There is a loss of electron occupancy from localized filled Lewis NBO into an empty antibonding non-Lewis orbital because of the nature of the interaction.[76] Calculated results for the interaction between the drug and the nanocage are presented in Table 4. From the NBO natural charges, pristine $Ca_{12}O_{12}$ has its Ca atoms to be electron-deficient (1.803e), while O atoms are electron-rich (−1.803e). Functionalization with the formyl group ($Ca_{12}O_{12}-CHO$) and the amino group ($Ca_{12}O_{12}-NH_2$) resulted in charge delocalization around the point of functionalization, i.e., Ca atoms possess charges of 1.799 and 1.723e and O atoms had charges of 1.798 and −1.191e in the $Ca_{12}O_{12}-CHO$ complex, while in the $Ca_{12}O_{12}-NH_2$ nanocage, the charges exhibited by Ca and O atoms around the point of functionalization are observed to be 1.811 and −1.560e respectively. However, adsorption of the 5FU drug on the surfaces of the nanocages resulted in significant charge transfer around the interaction areas as observed in $Ca_{12}O_{12}$ in which Ca atoms assumed charges of 1.811, 1.809, and 1.795e and O atoms similarly had charges of −1.151 and −1.792e. In the $Ca_{12}O_{12}-CHO$ complex, the charges on Ca atoms were calculated to be 1.810 and 1.805e, which are positive and similar to other systems, while the O atom maintained a charge of −1.757e. Similarly, the Ca atoms in the $Ca_{12}O_{12}-NH_2$ complex were observed to possess a net charge of 1.818e, while the O atoms assumed a negative charge between −1.396 and −1.784e. The calculated NBO values are presented in Tables 5 and S2 (Supporting Information). As

https://doi.org/10.1021/acsomega.2c03635
ACS Omega 2023, 8, 13551−13568

shown in Tables 5 and S2, an increase in $E^{(2)}$ energy was observed for $Ca_{12}O_{12}$−CHO and $Ca_{12}O_{12}$−NH_2 nanocages, which indicated a significant interaction between the functional groups and the pristine $Ca_{12}O_{12}$ complex. Furthermore, as laid out in Table S2, one can observe that the $E^{(2)}$ values for the studied complexes range from 9.98 to 282.80 kcal/mol. The following donor-to-acceptor interactions were found to be most significant: $\pi^*C_{25}-C_{28} \rightarrow \pi^*C_{27}-O_{35}(E^{(2)}$ = 121.01 kcal/mol) and LP (1) $N_{33} \rightarrow \pi^*C_{26}-O_{34}(E^{(2)}$ = 67.21 kcal/mol) for the complex $Ca_{12}O_{12}$; $\pi^*C_{28}-C_{31} \rightarrow \pi^*C_{30}-O_{38}(E^{(2)}$ = 100.34 kcal/mol) and LP*(1) $Ca_{18} \rightarrow$ LP*(1) $Ca_{20}(E^{(2)}$ = 61.65 kcal/mol) for the complex $Ca_{12}O_{12}$−CHO; and LP*(1) $Ca_{22} \rightarrow$ LP*(1) $Ca_{23}(E^{(2)})$ = 282.80 kcal/mol and LP*(1) $Ca_{19} \rightarrow$ LP*(1) Ca_{21} ($E^{(2)}$ = 250.78 kcal/mol) for the complex $Ca_{12}O_{12}$−NH_2. A large stabilization energy value indicates the stability of the isolated system resulting from a strong donor-to-acceptor intermolecular interaction. Hence, the system with the highest $E^{(2)}$ value is the most stable, and as such among the studied complexes, $Ca_{12}O_{12}$−NH_2 has the highest E^2 value of 282.80 kcal/mol and is thus considered to be the most stable complex based on this premise.

3.6. Frontier Molecular Orbital (FMO). To further understand the electronic interactions between the 5FU anticancer drug molecule and the pristine and functionalized $Ca_{12}O_{12}$ nanocages, FMO analysis was carried out. The FMOs were studied before and after the adsorption of the drug molecule. The FMO analysis is an important tool for understanding a system's electronic and optical properties.[77] The energy values for the highest occupied molecular orbital (E_{HOMO}), lowest unoccupied molecular orbital (E_{LUMO}), Fermi level energy (E_{FL}), and the highest occupied molecular orbital−lowest unoccupied molecular orbital (HOMO−LUMO) energy gap (E_g) in gas and water phases at the DFT/B3LYP-GD3BJ level are presented in Table S3 (Supporting Information), while the parameters in the gas phase are presented in Table 6. In addition, Figure 5 shows the graphical distribution of the HOMOs and LUMOs for the pristine, formyl-functionalized ($Ca_{12}O_{12}$−CHO), and amino-functionalized $Ca_{12}O_{12}$ ($Ca_{12}O_{12}$−NH_2) nanocages and their complexes, respectively. The HOMO−LUMO E_g was calculated in line with previous reports[63,83] However, the calculation of the energy gap gave insight into the stability, electron distribution, electrical conductivity, and sensitivity of all systems studied. A large energy gap indicates higher stability, lower sensitivity, lower electron energy distribution, and lower electrical conductivity of a system. The Fermi level energy E_{FL}, calculated at T = 0 K, occurred at the mid point of the HOMO−LUMO energy gap.[78,79]

Table 6. Highest Occupied MO Energy (E_{HOMO}), Lowest Unoccupied MO Energy (E_{LUMO}), Fermi Level Energy (E_{FL}), and the Energy Gap (E_g) Calculated at the DFT/B3LYP-GD3BJ/6-311++G (d, p) Level in the Gas Phase

system	E_{HOMO} (eV)	E_{LUMO} (eV)	E_{FL}(eV)	E_g (eV)
5FU	−7.32	−1.98	−4.66	5.33
$Ca_{12}O_{12}$	−5.09	−0.99	−3.04	4.09
$Ca_{12}O_{12}$−CHO	−2.54	−1.14	−1.84	1.39
$Ca_{12}O_{12}$−NH_2	−5.02	−1.04	−3.04	3.97
5FU@$Ca_{12}O_{12}$	−5.35	−1.14	−3.25	4.20
5FU@$Ca_{12}O_{12}$−CHO	−2.82	−1.69	−2.26	1.12
5FU@$Ca_{12}O_{12}$−NH_2	−5.46	−1.40	−3.44	4.06

As shown in Figure 5, the HOMO for pristine $Ca_{12}O_{12}$ is localized over the O atom of the nanocage, while the LUMO is equally distributed between the Ca and O atoms. However, formyl and amino functionalization ($Ca_{12}O_{12}$−CHO and $Ca_{12}O_{12}$−NH_2, respectively) caused a considerable change in the distribution pattern of the HOMO and LUMO in the pristine $Ca_{12}O_{12}$ nanocage. In $Ca_{12}O_{12}$−CHO, the HOMO is localized on the $Ca_{12}O_{12}$ nanocage, while the LUMO is localized on the −CHO group, indicating that there is a net charge transfer to the formyl group, whereas functionalization with the amino (−NH_2) group ($Ca_{12}O_{12}$−NH_2) demonstrated that the HOMO is primarily distributed on the NH_2 group. This suggests that the amino group is electron-rich and could not accommodate extra electrons from the $Ca_{12}O_{12}$ nanocage. Hence, the extra electrons spread to the nanocage at the LUMO level. Figure 5 also shows the HOMO and LUMO electron distribution after the adsorption of 5FU drug molecules on the nanocages. As laid out in Figure 6, it is pertinent that in $Ca_{12}O_{12}$ and $Ca_{12}O_{12}$−NH_2 complexes, the HOMO is majorly localized on the drug molecule, and the LUMO is distributed evenly on the $Ca_{12}O_{12}$ nanocages, whereas the $Ca_{12}O_{12}$−CHO complex shows that the HOMO is distributed across $Ca_{12}O_{12}$, while the LUMO electron density is localized on the −CHO group.

Based on the results in Table 6 and Table S3, the conclusion is that pristine $Ca_{12}O_{12}$ is a semiconductor with a large band gap, E_g (4.1 eV). The calculated E_g is similar to those previously reported.[64,67] The HOMO and LUMO energies of pristine $Ca_{12}O_{12}$ are about −5.1 and −0.9 eV, respectively. However, upon functionalization, the band gap and HOMO and LUMO energies change significantly. The computed HOMO and LUMO energies for $Ca_{12}O_{12}$−CHO are −2.5 and −1.1 eV, respectively, while those obtained for the $Ca_{12}O_{12}$−NH_2 complex are −5.0 and −1.0 eV, respectively. Similarly, the band gap in pristine $Ca_{12}O_{12}$ is reduced from 4.1 to 1.4 and 3.9 eV, in $Ca_{12}O_{12}$−CHO and $Ca_{12}O_{12}$−NH_2, respectively. These results indicated that functionalization of pristine CaO led to a decrease in the band gap, destabilization of the HOMO level, and stabilization of the LUMO level. It is worth noting that a decrease in the band gap leads to an increase in the electrical conductivity of systems.

The relationship between E_g and electrical conductivity can be described by the following equation[80]

$$\sigma \propto \exp\left(\frac{-E_g}{kT}\right) \tag{3}$$

where σ is defined as the electric conductivity, k is the Boltzmann constant, and T is the temperature expressed in Kelvin. Therefore, $Ca_{12}O_{12}$−CHO, with an E_g of 1.4 eV, is observed to have the highest electrical conductivity and is a better semiconductor when compared with pristine $Ca_{12}O_{12}$ and $Ca_{12}O_{12}$−NH_2. The destabilization of the HOMO and stabilization of the LUMO results in the formation of new Fermi level energy values for both functionalized $Ca_{12}O_{12}$−CHO and $Ca_{12}O_{12}$−NH_2.

Furthermore, as laid out in Table 6, it is obvious that the E_g of pristine $Ca_{12}O_{12}$ and $Ca_{12}O_{12}$−CHO decreased after the adsorption of the drug molecule and the change is most obvious in $Ca_{12}O_{12}$−CHO. The band gaps of $Ca_{12}O_{12}$−CHO are computed to be 4.1 and 1.1 eV. This decrease in E_g is an indicator of improved conductivity.

https://doi.org/10.1021/acsomega.2c03635
ACS Omega 2023, 8, 13551−13568

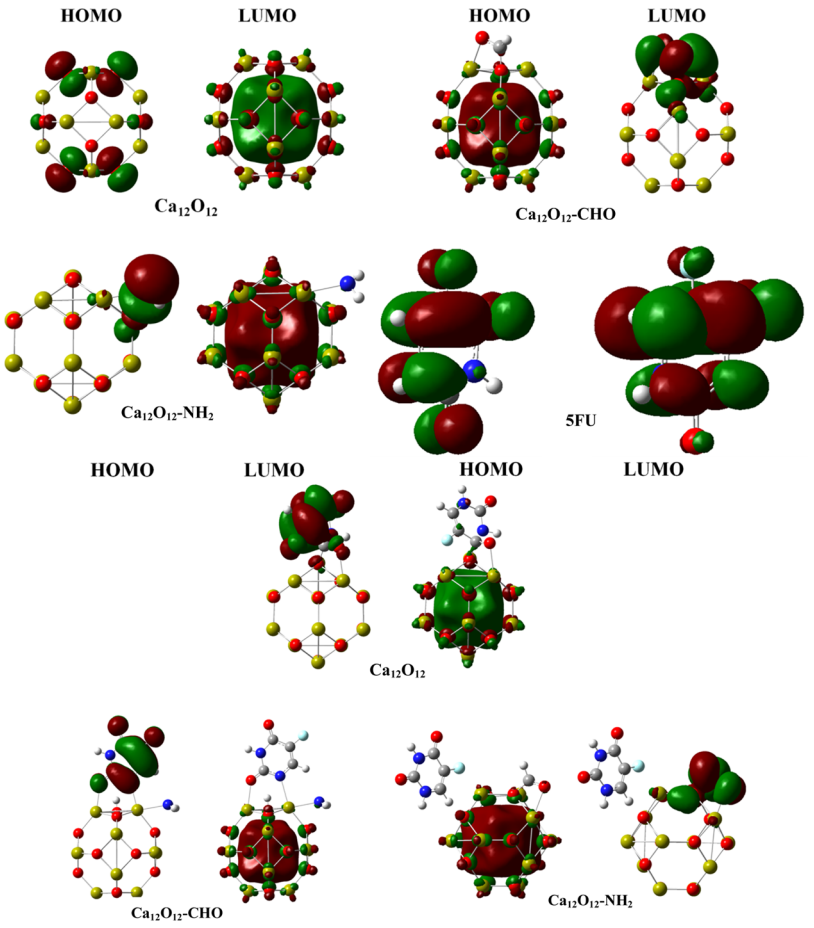

Figure 5. HOMO−LUMO plots for the nanocages.

3.7. Global Reactivity Descriptors. To investigate the stability and reactivity of the pristine and functionalized $Ca_{12}O_{12}$ nanocages toward the 5FU drug, global reactivity descriptors were considered according to the generalized Koopmans' theorem.[81] The ionization potential (IP) and electron affinity (EA) are equivalent to the inverse of the HOMO and LUMO energies, respectively. However, other reactivity descriptors like the chemical potential (μ), electronegativity (χ), global hardness (η), electrophilicity index (ω), and global softness (S)[82] were also calculated. The calculated global reactivity descriptors are tabulated in Table 7, which conveniently supply the necessary information needed to accurately predict the stability and reactivity of each studied system. Interestingly, the global hardness gives insight into the ability of a chemical species to resist electron charge transfer within its environment. A low value of global hardness and ionization potential indicates the low stability and high reactivity of a system, whereas high values for global softness are associated with high stability and low reactivity.[83−86]

From Table 7, the computed global hardness values were observed to be 2.3, 0.698, and 1.9 eV, and the ionization potential values were calculated to be 5.1, 2.5, and 5.0 eV for pristine $Ca_{12}O_{12}$, $Ca_{12}O_{12}$−CHO, and $Ca_{12}O_{12}$−NH_2, nanocages, respectively. However, after adsorption of the 5FU drug on the nanocages, the respective hardness and ionization potential increased in the case of $Ca_{12}O_{12}$ (5.4 and 2.1 eV), 5FU@$Ca_{12}O_{12}$−CHO (2.8 and 0.6 eV), and 5FU@$Ca_{12}O_{12}$−NH_2 (5.5 and 2.0 eV). These results indicated that stability increased while reactivity decreased. Nonetheless, the complex 5FU@$Ca_{12}O_{12}$−CHO was observed to have the least hardness and ionization potential values, which disclosed it to have the lowest stability and highest reactivity. Meanwhile, the highest IP was observed in 5FU@$Ca_{12}O_{12}$−NH_2 (the most stable and least reactive complex). The electronegativity values obtained for the complexes 5FU@$Ca_{12}O_{12}$, 5FU@$Ca_{12}O_{12}$−CHO, and 5FU@$Ca_{12}O_{12}$−NH_2 were 3.3, 3.4, 2.3, and 3.4 eV, respectively. The highest electronegativity values were noted in 5FU@$Ca_{12}O_{12}$−NH_2, which suggested that the two complexes had the highest stability.

Furthermore, Table 7 shows that adsorption of the 5FU drug increased the electrophilicity index values for all nanocages, which signified an increase in electrophilic character for all complexes, since the electrophilicity index gives a measure of the stabilization energy obtained when a chemical species gains an additional amount of electrons[87] The calculated results, however, indicated that the complex 5FU@$Ca_{12}O_{12}$−CHO (ω = 4.5 eV) is the strongest electrophile, while the complex 5FU@$Ca_{12}O_{12}$ (ω = 2.5 eV) is the strongest nucleophile. Similarly, the highest electron affinity is observed in the complex 5FU@$Ca_{12}O_{12}$−CHO. In addition, the softness for the $Ca_{12}O_{12}$−CHO nanocage (0.7 eV) shifted to a higher value, while the $Ca_{12}O_{12}$−NH_2 nanocage (0.3 eV) had no significant change in value compared to pristine $Ca_{12}O_{12}$ (0.2 eV). The same is observed after the adsorption of the 5FU drug on the nanocages. That is, the softness of the formyl-functionalized complex 5FU@$Ca_{12}O_{12}$−CHO was calculated to be 0.9 eV, while for other complexes, 5FU@$Ca_{12}O_{12}$ and 5FU@$Ca_{12}O_{12}$−NH_2, softness was calculated to be 0.2, 0.2,

https://doi.org/10.1021/acsomega.2c03635
ACS Omega 2023, 8, 13551−13568

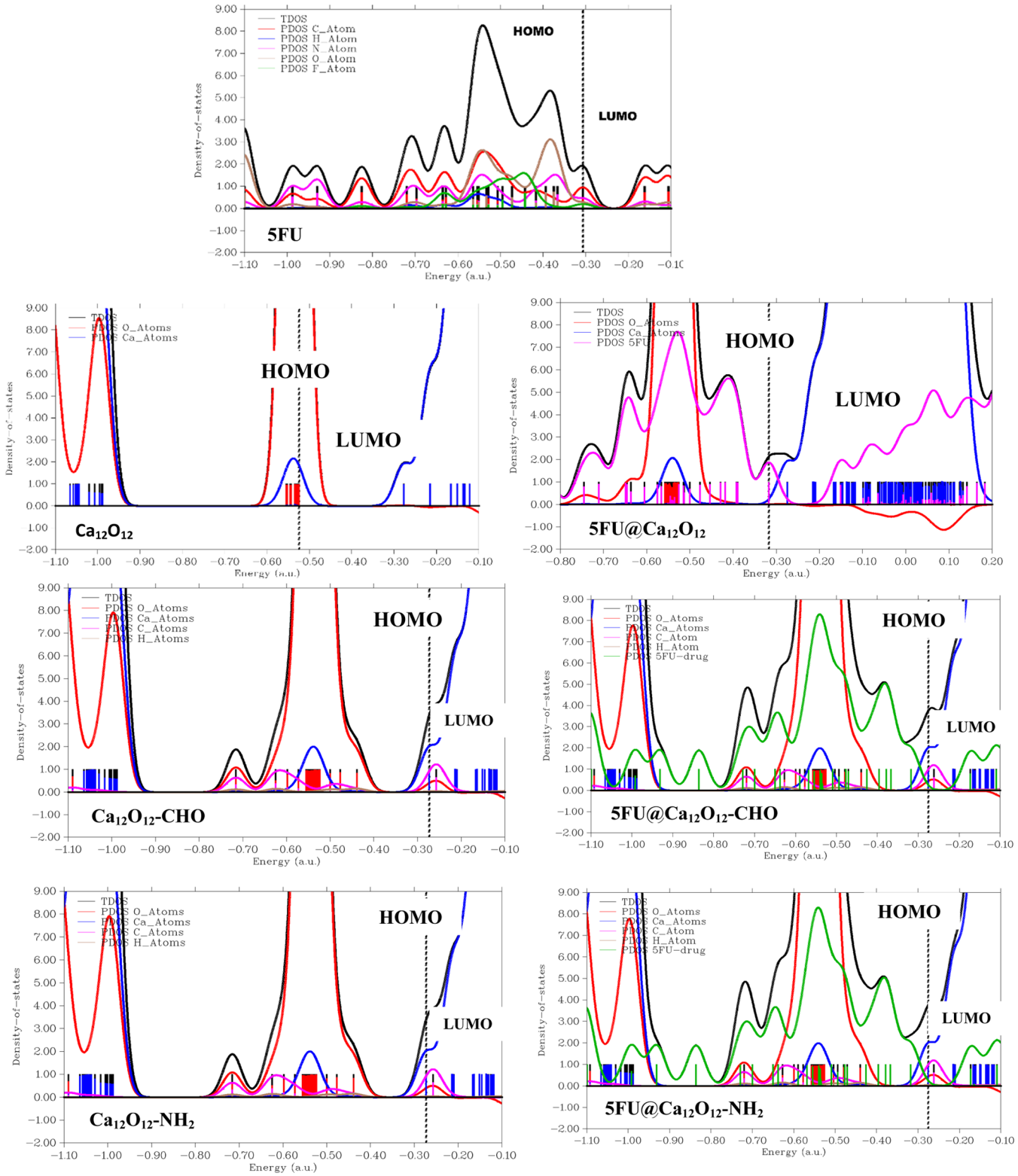

Figure 6. Projected density of states (DOS) maps for the studied complexes.

and 0.2 eV, respectively. These results further corroborate that the complex 5FU@$Ca_{12}O_{12}$−CHO, with the highest softness value out of all studied systems, has the highest reactivity and least stability. Above all, large ionization potential and global hardness values with small global softness values in the complexes 5FU@$Ca_{12}O_{12}$ and 5FU@$Ca_{12}O_{12}$−NH_2 suggest that these systems are quite stable with minimum reactivity compared with the complex 5FU@$Ca_{12}O_{12}$−NH_2, which is the most reactive and least stable system.

3.8. Density of States (DOS). The DOS analysis gave further insight into the electronic distribution patterns of the frontier molecular orbitals in both occupied and vacant energy states. It also aids in revealing possible charge transfer as well as shifting the band structure as a result of the adsorption of

https://doi.org/10.1021/acsomega.2c03635
ACS Omega 2023, 8, 13551−13568

Table 7. Calculated Quantum Descriptors of the Studied Systems Computed at the B3LYP-GD3(BJ)/6-311++(d,p) Level[a]

system	IP	EA	χ	M	η	S	ω
5FU	7.3	1.9	4.7	−4.7	2.7	0.2	4.1
$Ca_{12}O_{12}$	5.1	0.9	3.0	−3.0	2.0	0.2	2.3
$Ca_{12}O_{12}$−CHO	2.5	1.1	1.8	−1.8	0.7	0.7	2.4
$Ca_{12}O_{12}$−NH_2	5.0	1.0	3.0	−3.0	1.9	0.3	2.3
5FU@$Ca_{12}O_{12}$	5.4	1.1	3.2	−3.3	2.1	0.2	2.5
5FU@$Ca_{12}O_{12}$−CHO	2.8	1.7	2.3	−2.3	0.6	0.9	4.5
5FU@$Ca_{12}O_{12}$−NH_2	5.5	1.4	3.4	−3.4	2.0	0.2	2.9

[a]Ionization potential (IP, eV), electron affinity (EA, eV), electronegativity (χ, eV), chemical potential (μ, eV), global hardness (η, eV), global softness (S, eV^{-1}), and electrophilic index (ω, eV).

adsorbent molecules. The obtained densities of states and projected densities of states are presented in Figure 6; the overlap partial DOS (OPDOS) is positioned on the right side of the DOS graph, while the total DOS (TDOS) and partial DOS (PDOS) are positioned on the left side of the graph. For all systems, the Fermi level (E_F) position is represented by the vertical dashed line on the graph. It is observed from the figure that the HOMO and LUMO in the pristine $Ca_{12}O_{12}$ nanocage are equally distributed. However, amino (−NH_2, $Ca_{12}O_{12}$−NH_2) and formyl (−CHO, $Ca_{12}O_{12}$−CHO) functionalization resulted in a charge transfer between pristine $Ca_{12}O_{12}$ and the functional groups. In addition, from the graph for the complexes 5FU@$Ca_{12}O_{12}$, 5FU@$Ca_{12}O_{12}$−CHO, and 5FU@$Ca_{12}O_{12}$−NH_2, it is ostensible that the major contributions to the frontier molecular orbitals in both occupied and vacant states are dominated by both calcium and oxygen atoms of the nanocage as well as the drug molecule. However, the occupied states in the nanocages before adsorption are dominated by contributions from only the nanocluster with only minimal contributions from the oxygen and calcium atoms. Nonetheless, a greater contribution from the drug fragment is observed, which clearly indicates that the charge was transferred from the drug to the nanocluster and vice versa.

3.9. Quantum Theory of Atoms in Molecules (QTAIM). The quantum theory of atoms in molecules, derived from Bader's theory for topology analysis,[60] is a useful tool for determining inter- or intramolecular interactions. Chemical bonds, including hydrogen bonding, are characterized by the existence of bond critical points (BCPs). The nature of the interaction between molecules is also explained by this hypothesis.[87,88] Several topological parameters can be calculated after BCP localization including the density of all electrons $\rho(\mathbf{r})$, Laplacian of electron density $\nabla^2 p(\mathbf{r})$, Lagrangian of kinetic energy $G(\mathbf{r})$, Hamiltonian kinetic energy $K(\mathbf{r})$, potential energy density $V(\mathbf{r})$, energy density $H(\mathbf{r})$, electron localization function (ELF), Eigenvalues (λ_1, λ_2, λ_3), and ellipticity, ε. The different topological properties, obtained at the DFT/B3LYP-GD3 (BJ) with 6-311++ (d,p) level, are listed in Table 8. However, a graphical illustration is presented in Figure 7. In this work, QTAIM was employed to analyze the characteristics of the intermolecular hydrogen bond by studying critical points existing between the drug molecule and the nanocages during interactions. The strength of a chemical bond is determined by values of the density, $\rho(\mathbf{r})$, wherein the highest value of $\rho(\mathbf{r})$ shows the strongest chemical bond, while the lowest $\rho(\mathbf{r})$ values indicate the weakest chemical bond.[89−91] From Table 8, the highest $\rho(\mathbf{r})$ value of 0.0430 a.u. is observed for the 5FU@$Ca_{12}O_{12}$−CHO complex, which depicts a strong chemical bond between the nanocage and the drug molecule. Other values for the $\rho(\mathbf{r})$ range from 0.0055 to 0.0394 a.u. Negative values for $\nabla^2(\mathbf{r})$ and $H(\mathbf{r})$ indicate strong covalent interactions, whereas the positive values of $\nabla^2(\mathbf{r})$ and negative values of $H(\mathbf{r})$ indicate medium interactions (partially covalent). Furthermore, when both values are positive ($\nabla^2(\mathbf{r}) > 0$ and $H(\mathbf{r}) > 0$), they show weak (noncovalent) interactions.[92] The binding energy values from Table 8 divulged that 5FU@$Ca_{12}O_{12}$−CHO and 5FU@$Ca_{12}O_{12}$ complexes upon interaction with the 5FU drug is highly stable following the high binding energies of −51.6 and −44.9 kcal/mol at O_{27}−C_{24} and O_{10}−C_{27} bond critical points (BCPs), respectively, which is in accordance to several literature claims, asserting that the larger the value of the mass defect, the greater and more effective the nuclear binding energy as well as the more stable the nucleus would be. However, the binding energy for 5FU@$Ca_{12}O_{12}$−NH_2 suggests that these molecules are likely to be unstable upon the adsorption of the 5FU drug. As such the Laplacian of electron density for each BCP was observed to be 0.0952 at Ca_{15}−N_{33} BCP and −0.2413 at O_{10}−C_{27} BCP for the $Ca_{12}O_{12}$ system; the same trend was observed for the $Ca_{12}O_{12}$−CHO molecule, as its ∇^2Pbcp was observed to be 0.1636 at O_3−H_{32} BCP and 0.3173 at O_{27}−C_{24} BCP. It was further observed that electrostatic interaction was dominant for the $Ca_{12}O_{12}$−NH_2 molecule with a ∇^2Pbcp of 0.1853 at Ca_{10}−O_{34} BCP. Interestingly, owing to these results, covalent interactions were observed between Ca_{15}−N_{33} and O_{27}−C_{24} BCPs for 5FU@$Ca_{12}O_{12}$- and 5FU@$Ca_{12}O_{12}$−CHO-adsorbed systems. respectively, due to the presence of negative Laplacian of electron density at respective critical points, which is in tandem with the high binding energy observed for the said molecules. The result further elucidates that electrostatic interaction was also dominant in the 5FU@$Ca_{12}O_{12}$−NH_2 investigated compound as explicated by the presence of the positive Laplacian of electron density (∇^2Pbcp). Also, the result reveals that electron density is comparably greater at Ca_{15}−N_{33} and O_{33}−H_{32} BCPs for 5FU@$Ca_{12}O_{12}$ and 5FU@$Ca_{12}O_{12}$−CHO systems, respectively, and less concentrated at Ca_{10}—O_{34} and Ca_{14}—N_{35} BCPs for the 5FU@$Ca_{12}O_{12}$−NH_2 compound. Thus, the result obtained herein agrees with the electronic studies of the said molecules, as the $Ca_{12}O_{12}$ system was observed to possess the highest energy gap of 4.2 eV and nucleophilicity (HOMO) of −5.4 eV, elucidating that the studied $Ca_{12}O_{12}$ system is comparably highly stable upon adsorption of 5FU. Ellipticity (ε) can be mathematically expressed as $\varepsilon = \lambda_1/\lambda_{2-1}$ where λ_1 and λ_2 designate the negative Hessian of electron density at BCPs and can be grouped in the order of increasing preference as $\lambda_3 > 0 > \lambda_2 > \lambda_1$. The measure of the anisotropy of the curvature of the electron density in the direction considered normal to the bond is represented by the ellipticity parameter. Thus, the parallel expansion λ_1/λ_2 and the

https://doi.org/10.1021/acsomega.2c03635
ACS Omega 2023, 8, 13551−13568

Table 8. Calculated Topological Parameters: Electron Density $\rho(\mathbf{r})$, Laplacian Electron Density $\nabla^2(\mathbf{r})$, Lagrangian Kinetic Energy $G(\mathbf{r})$, Hamiltonian Kinetic Energy $K(\mathbf{r})$, Potential Electron Energy Density $V(\mathbf{r})$, Total Electron Energy Density $H(\mathbf{r})$, $-G(\mathbf{r})/V(\mathbf{r})$ Ratio at Bond Critical Points (BCPs), Electron Localization Function (ELF), Eigenvalues (λ_1, λ_2, λ_3), and Ellipticity (ε) of the Studied Complexes[a]

system	parameters	bond	binding energy (kcal/mol)	$\rho(\mathbf{r})$	$\nabla^2 p(\mathbf{r})$	$G(\mathbf{r})$	$K(\mathbf{r})$	$V(\mathbf{r})$	$H(\mathbf{r})$	$-G(\mathbf{r})/V(\mathbf{r})$	ELF	λ_1	λ_2	λ_3	λ_1/λ_3	ε
5FU@$Ca_{12}O_{12}$	BE(E_{Ca-N})	Ca_{15}–N_{33}	−4.66	0.024	0.095	0.021	−0.002	−0.019	0.002	1.1263	0.0694	0.1437	−0.024	−0.0248	−5.79	0.0469
	BE(E_{O-C})	O_{10}–C_{27}	−44.99	0.231	−0.241	0.229	0.289	−0.519	−0.289	0.4416	0.5414	0.5925	−0.442	−0.3919	−1.38	0.1276
	BE(E_{Ca-O})	Ca_{14}–O_{35}	−8.52	0.042	0.209	0.048	−0.005	−0.043	0.005	1.1124	0.0831	0.3103	−0.048	−0.0530	−5.85	0.1068
	BE(E_{Ca-F})	Ca_{16}–F_{36}	−3.65	0.019	0.092	0.020	−0.003	−0.018	0.003	1.1468	0.0393	0.1357	−0.023	−0.0211	−6.43	0.0643
5FU@$Ca_{12}O_{12}$–CHO	BE(E_{O-H})	O_3–H_{32}	−8.85	0.0430	0.1636	0.0418	0.0009	−0.0427	−0.0009	0.9789	0.1166	0.2985	−0.0673	−0.0675	−4.42	0.2264
	BE(E_{Ca-F})	Ca_{16}–F_{39}	−4.05	0.0215	0.1067	0.0232	−0.0034	−0.0198	0.0034	1.1717	0.0407	0.1568	−0.026	−0.0243	−6.45	0.0577
	BE(E_{O-C})	O_{27}–C_{24}	−51.64	0.2348	−0.3173	0.2165	0.2958	−0.5123	−0.2958	0.4226	0.5843	−0.3961	0.570	−0.4917	0.81	0.2414
	BE(E_{Ca-O})	Ca_{17}–O_{26}	−8.05	0.0394	0.1962	0.0441	−0.0049	−0.0392	0.0049	1.1250	0.0811	−0.0481	0.294	−0.0497	0.96	0.0334
5FU@$Ca_{12}O_{12}$–NH_2	BE(E_{Ca-O})	Ca_{16}–O_{34}	−7.27	0.0359	0.1853	0.0409	−0.0053	−0.0356	0.0053	1.1488	0.0701	0.2713	−0.044	−0.0425	−6.38	0.0236
	BE(E_{Ca-N})	Ca_{14}–N_{35}	−5.82	0.0294	0.1129	0.0259	−0.0022	−0.0236	0.0022	1.0974	0.0882	0.1765	−0.033	−0.0307	−5.75	0.0696
	BE(E_{N-H})	N_{24}–H_{32}	−0.48	0.006	0.016	0.003	−0.001	−0.003	0.0006	1.2592	0.0205	0.0250	−0.004	−0.0047	−5.32	0.2045
	BE(E_{Ca-N})	Ca_{14}–N_{24}	−7.58	0.037	0.154	0.036	−0.002	−0.034	0.0022	1.0674	0.0972	−0.0398	0.237	−0.0429	0.93	0.0789
	BE(E_{O-N})	O_7–N_{24}	−6.12	0.030	0.136	0.031	−0.003	−0.028	0.0031	1.1151	0.0723	0.1905	−0.024	−0.0298	−6.39	0.2525

[a]All of the values are in a.u.

https://doi.org/10.1021/acsomega.2c03635
ACS Omega 2023, 8, 13551−13568

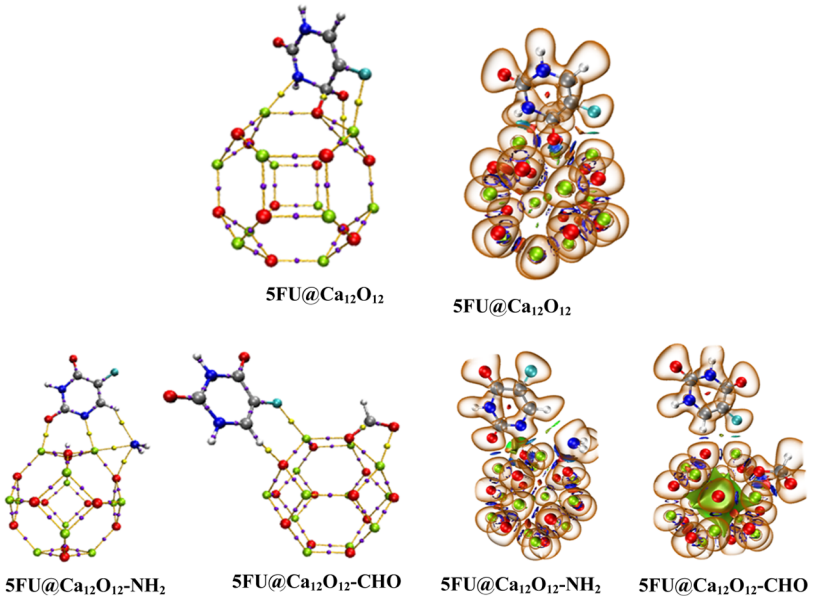

Figure 7. Left side—QTAIM molecular graphs for all studied complexes. The yellow- and violet-colored points designate the bond critical points (BCPs) within and outside the nanocage structure. The green, red, silver, white, blue, and cyan balls represent Ca, O, C, H, N, and F atoms, respectively. Right side—a combined plot of the NCI isosurface and ELF for all complexes.

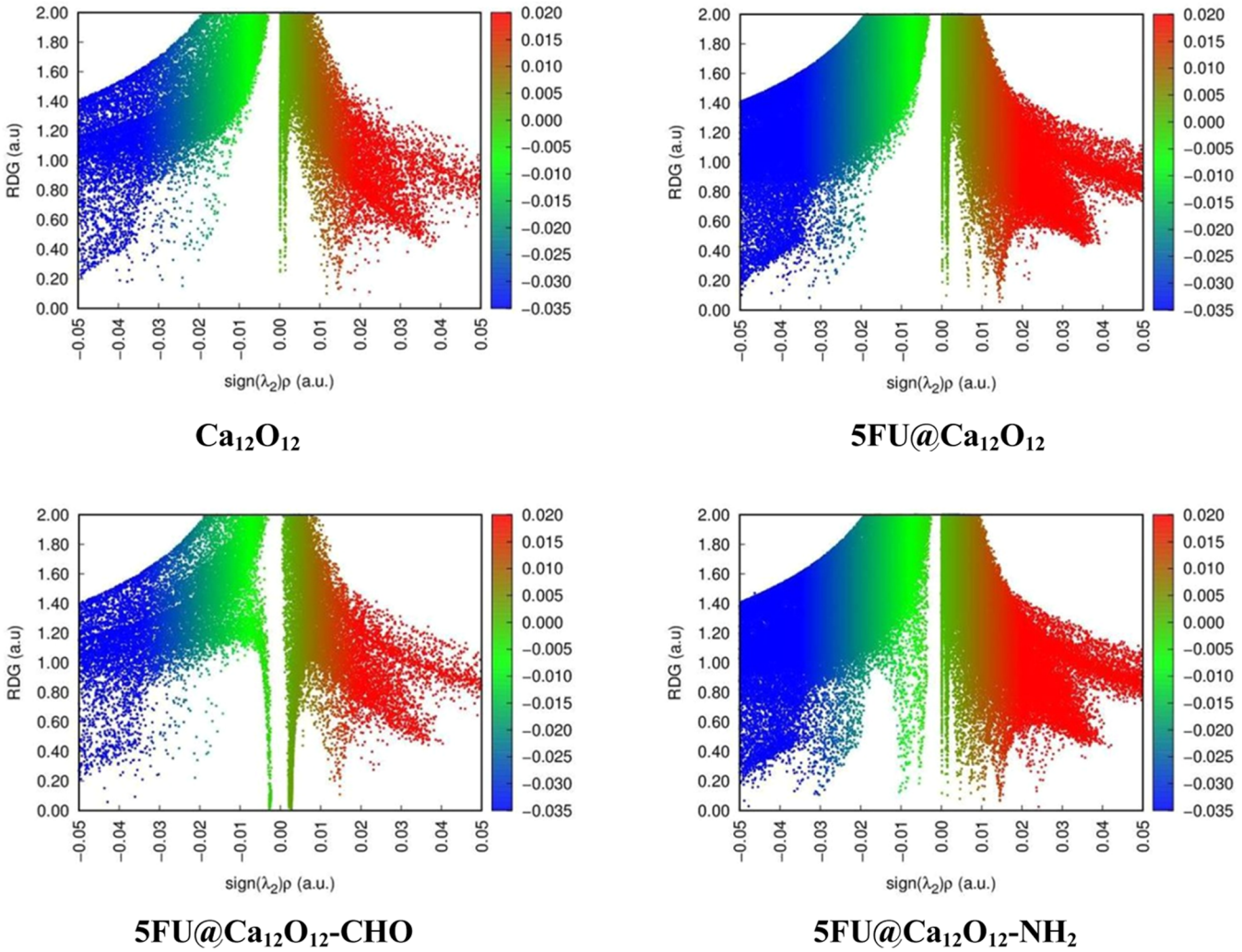

Figure 8. Reduced density gradient scatter maps for all studied complexes.

https://doi.org/10.1021/acsomega.2c03635
ACS Omega 2023, 8, 13551−13568

ellipticity value for all systems are observed to be less than 1, depicting a very strong intermolecular interaction between the adsorbate and the adsorbent species; hence, the adsorption process of the investigated molecules upon interaction with the drug molecule was highly favorable.

3.10. Noncovalent Interaction (NCI) Analysis. The NCI analysis was employed to further reveal the nature of the weak interactions that exist between the drug molecule and the nanocages.[97] For these analyses, a graph of the reduced density gradient (RDG) versus the second eigenvalue of the electron density Hessian matrix (λ_2) and the electron density in atomic unit ρ(a.u) (RDG against sign $\lambda_2(\mathbf{r})\rho(\mathbf{r})$) was plotted and visualized using the VMD program. The resulting scatter map is presented in Figure 8, while a combined reduced density gradient (RDG) and electron localization function (ELF) isosurface plot is presented in Figure 8 for all studied complexes. Using a blue-green-red index scale, the weak interactions can be interpreted. The blue region with negative values (sign (λ_2) $\rho < 0$) corresponds to strong interactions (such as hydrogen bonding) and high electron density, while the red region with positive values (sign (λ_2) $\rho > 0$) indicates a strong repulsive interaction (like steric effect) and electron density depletion; the green region (sign (λ_2) $\rho \approx 0$) corresponds to relatively weak van der Waal (vdW) interactions.[93,94]

As evident from the plots in Figures 7 and 8, the blue regions existing between the 5FU drug and the nanocages, for all complexes, indicate the presence of strong hydrogen bonding interactions. However, deeper colorations observed in Figure 8 for 5FU@$Ca_{12}O_{12}$ and 5FU@$Ca_{12}O_{12}$−NH_2 indicate that these complexes possess high electron density. The green region observed between the 5FU drug and the nanocage in the complex 5FU@$Ca_{12}O_{12}$−NH_2 indicates that vdW interactions play a key role in the drug adsorption for this complex. In addition, little repulsion interaction is observed in the complex $Ca_{12}O_{12}$, which results from the steric effect (due to the ring orientation) during the adsorption process. These are in good agreement with the adsorption energy and the QTAIM results.

3.11. Electron Localization Function (ELF). Another essential parameter for analyzing covalent bonding is the electron localization function. An ELF value ranging between 0.5 and 1 a.u. suggests regions with bonding and nonbonding localized electrons, whereas an ELF value that is less than 0.5 indicates delocalized electrons.[95] As can be visualized from Figure 7, the ELF values for the 5FU@$Ca_{12}O_{12}$−NH_2 complex indicate the delocalization of electrons.[96] However, other bond interactions between the drug molecule and the nanocage suggest bonding and nonbonding localized electrons as the values exist between 0.5 and 1 for all hydrogen bonds, while $|\lambda_1|/\lambda_3$ values are found to fall within the range of 0.5−1. On the basis of $|\lambda_1|/\lambda_3$, the strongest hydrogen bonds are observed for O_{10}−C_{27} in the $Ca_{12}O_{12}$ complex (0.5925 a.u.), while the weakest hydrogen bond is observed for Ca_{14}−N_{24} (−0.0398 a.u.) in the complex 5FU@$Ca_{12}O_{12}$−NH_2. From these results, we can conclude that with strong chemical bond interaction, hydrogen bond interaction, and low values observed for ε, the studied nanocages are generally stable and suitable for drug delivery.

4. CONCLUSIONS

In this work, the potential of $Ca_{12}O_{12}$ nanocluster as an effective nanovehicle for 5-fluorouracil (5FU) and its functionalized derivatives has been explored at the DFT/B3LYP-GD3(BJ)/6-311++ G(d,p) level of theory. The geometrical, adsorption energy, dipole moment, molecular electrostatic potential, natural bond orbital, frontier molecular orbital, density of state, global reactivity descriptors, topological (QTAIM), ELF, and NCI analyses were explored to assess the suitability of the modeled nanoclusters as drug nanovehicles for 5FU. However, the calculations revealed that the 5FU drug was adsorbed favorably in all of the complexes with calculated adsorption energies of −136.8, −97.5, and −175.6 kcal/mol, respectively, for 5FU@$Ca_{12}O_{12}$, 5FU@$Ca_{12}O_{12}$−CHO, and 5FU@$Ca_{12}O_{12}$−NH_2, respectively. Interestingly, the results divulged that the adsorption nature of the 5FU drug was influenced by its geometrical orientation to the nanocages as well as the adsorption energies. Solvation effects also contributed significantly to the molecular properties of the studied systems. Most complexes were observed to possess a higher electronegativity index in the gas phase than that in the water phase. Similarly, QTAIM and NCI calculations showed that hydrogen bonding facilitated the interaction between the 5FU drug and all nanocages. Most importantly, van der Waals forces were also observed to have contributed to the interaction of 5FU with the 5FU@$Ca_{12}O_{12}$−NH_2 complex. However, the FMO calculations revealed that the complex 5FU@$Ca_{12}O_{12}$−CHO (E_g = 1.1 eV) with the least energy gap has comparably higher conductivity and least stability. Nevertheless, the results showed that other modeled complexes had larger energy gaps (E_g), and the $Ca_{12}O_{12}$ complex was observed to be the most stable of all with an E_g of 4.2 eV, while the 5FU@$Ca_{12}O_{12}$−NH_2 system appeared to be the best complex due to its conductivity, high stability, and adsorption energy as clearly depicted by the energy gap (E_g) of 4.1 eV. The global reactivity studies of the modeled systems suggest that the complex 5FU@$Ca_{12}O_{12}$−CHO with comparably higher reactivity is thus the strongest electrophile due to the small energy gap, low hardness, low ionization potential, and high electrophilicity index. Also, the NBO analysis revealed a charge transfer from the 5FU drug to the Ca atoms of the nanocages. Thus, based on the results obtained from this theoretical investigation, pristine and amino-functionalized $Ca_{12}O_{12}$ nanocages are promising drug delivery candidates for the 5FU anticancer drug.

■ ASSOCIATED CONTENT

Data Availability Statement

All data are contained within the manuscript and manuscript supporting information document (ESI).

Supporting Information

The Supporting Information is available free of charge at https://pubs.acs.org/doi/10.1021/acsomega.2c03635.

Selected bond lengths of the studied drug molecule before and after interaction (Table S1); calculated second-order perturbation energies of the studied complexes obtained at the DFT B3LYP-GD3BJ/6-311++G(d,p) level (Table S2); calculated quantum chemical descriptors for the studied complexes obtained in gas and water (Table S3); calculated BSSE energies and complexation energies of the studied systems (Table S4); calculated dipole moments of the studied complexes in gas and water (Table S5); tabulated *XYZ* coordinates for the interacted complexes (Tables S6−

https://doi.org/10.1021/acsomega.2c03635
ACS Omega 2023, 8, 13551−13568

S8), and other adsorbed configurations of 5FU with $Ca_{12}O_{12}$ (Figure S1) (PDF)

AUTHOR INFORMATION

Corresponding Authors

Hitler Louis − *Computational and Bio-Simulation Research Group, University of Calabar, Calabar 540221, Nigeria; Department of Pure and Applied Chemistry, Faculty of Physical Sciences, University of Calabar, Calabar 540221, Nigeria;* orcid.org/0000-0002-0286-2865; Email: louismuzong@gmail.com

Adedapo S. Adeyinka − *Department of Chemical Sciences, University of Johannesburg, Johannesburg 2006, South-Africa*; Email: aadeyinka@uj.ac.za

Authors

Goodness J. Ogunwale − *Computational and Bio-Simulation Research Group, University of Calabar, Calabar 540221, Nigeria; Department of Chemistry, Faculty of Science, University of Ibadan, Ibadan 200005, Nigeria*

Tomsmith O. Unimuke − *Computational and Bio-Simulation Research Group, University of Calabar, Calabar 540221, Nigeria; Department of Pure and Applied Chemistry, Faculty of Physical Sciences, University of Calabar, Calabar 540221, Nigeria;* orcid.org/0000-0001-8721-2345

Gideon E. Mathias − *Computational and Bio-Simulation Research Group, University of Calabar, Calabar 540221, Nigeria; Department of Pure and Applied Chemistry, Faculty of Physical Sciences, University of Calabar, Calabar 540221, Nigeria*

Aniekan E. Owen − *School of Chemistry, University of St Andrews, St Andrews KY16 9ST, Scotland*

Henry O. Edet − *Computational and Bio-Simulation Research Group, University of Calabar, Calabar 540221, Nigeria; Department of Pure and Applied Chemistry, Faculty of Physical Sciences, University of Calabar, Calabar 540221, Nigeria*

Obieze C. Enudi − *Computational and Bio-Simulation Research Group, University of Calabar, Calabar 540221, Nigeria; Department of Chemistry, Faculty of Science, University of Ibadan, Ibadan 200005, Nigeria;* orcid.org/0000-0001-6306-2047

Esther O. Oluwasanmi − *Computational and Bio-Simulation Research Group, University of Calabar, Calabar 540221, Nigeria; Department of Chemistry, Faculty of Science, University of Ibadan, Ibadan 200005, Nigeria;* orcid.org/0000-0003-4855-2413

Mohsen Doust Mohammadi − *School of Chemistry, College of Science, University of Tehran, Tehran 14176, Iran;* orcid.org/0000-0003-2449-2962

Complete contact information is available at: https://pubs.acs.org/10.1021/acsomega.2c03635

Author Contributions

H.L.: project conceptualization, design, and supervision. G.J.O.: writing, result extraction, analysis, and manuscript first draft. T.O.U.: validation, methodology, writing, and manuscript review and editing. G.E.M.: manuscript revision. A.E.O.: analysis. H.O.E.: writing and editing. E.C.O. and E.E.O.: writing, editing, and analysis. M.D.M. and A.A.: resources, review, and editing.

Funding

This research was not funded by any governmental or non-governmental agency.

Notes

The authors declare no competing financial interest.
All authors declare zero financial or interpersonal conflict of interest that could have influenced the research work or results reported in this research paper.

ACKNOWLEDGMENTS

The authors would like to acknowledge the Center for High Performance Computing (CHPC), South Africa for providing computational resources for this research project. Also, G.J.O. especially acknowledges H.L. and G.K.O. for their immense support during this research.

REFERENCES

(1) https://www.who.int/news-room/fact-sheets/detail/cancer. Accessed May 12, 2022.
(2) https://www.who.int/health-topics/cancer#tab=tab_1. Accessed May 12.
(3) Longley, D. B.; Harkin, D. P.; Johnston, P. G. 5-fluorouracil: mechanisms of action and clinical strategies. *Nat. Rev. Cancer* **2003**, *3*, 330−338.
(4) https://en.wikipedia.org/wiki/Fluorouracil. Accessed May 12.
(5) Zhang, N.; Yin, Y.; Xu, S.-J.; Chen, W.-S. 5-Fluorouracil: mechanisms of resistance and reversal strategies. *Molecules* **2008**, *13*, 1551−1569.
(6) Blondy, S.; David, V.; Verdier, M.; Mathonnet, M.; Perraud, A.; Christou, N. 5-Fluorouracil resistance mechanisms in colorectal cancer: From classical pathways to promising processes. *Cancer Sci.* **2020**, *111*, 3142−3154.
(7) Xie, P.; Mo, J.-L.; Liu, J.-H.; Li, X.; Tan, L.-M.; Zhang, W.; Zhou, H.-H.; Liu, Z.-Q. Pharmacogenomics of 5-fluorouracil in colorectal cancer: review and update. *Cell. Oncol.* **2020**, *43*, 989−1001.
(8) Guimarães, D.; Cavaco-Paulo, A.; Nogueira, E. Design of liposomes as drug delivery system for therapeutic applications. *Int. J. Pharm.* **2021**, *601*, No. 120571.
(9) El-Hammadi, M. M.; Arias, J. L. An update on liposomes in drug delivery: a patent review (2014-2018). *Expert Opin. Ther. Pat.* **2019**, *29*, 891−907.
(10) Jana, P.; Shyam, M.; Singh, S.; Jayaprakash, V.; Dev, A. Biodegradable polymers in drug delivery and oral vaccination. *Eur. Polym. J.* **2021**, *142*, No. 110155.
(11) George, A.; Shah, P. A.; Shrivastav, P. S. Natural biodegradable polymers-based nano-formulations for drug delivery: A review. *Int. J. Pharm.* **2019**, *561*, 244−264.
(12) Rajani, C.; Borisa, P.; Karanwad, T.; Borade, Y.; Patel, V.; Rajpoot, K.; Tekade, R. K.Cancer-Targeted Chemotherapy: Emerging Role of the Folate Anchored Dendrimer as Drug Delivery Nanocarrier. In *Pharmaceutical Applications of Dendrimers*; Elsevier, 2020; pp 151−198.
(13) Nikzamir, M.; Hanifehpour, Y.; Akbarzadeh, A.; Panahi, Y. Applications of dendrimers in nanomedicine and drug delivery: A review. *J. Inorg. Organomet. Polym. Mater.* **2021**, *31*, 2246−2261.
(14) Khan, A. U.; Khan, M.; Cho, M. H.; Khan, M. M. Selected nanotechnologies and nanostructures for drug delivery, nanomedicine and cure. *Bioprocess Biosyst. Eng.* **2020**, *43*, 1339−1357.
(15) Henna, T.; Raphey, V.; Sankar, R.; Shirin, V. A.; Gangadharappa, H.; Pramod, K. Carbon nanostructures: The drug and the delivery system for brain disorders. *Int. J. Pharm.* **2020**, *587*, No. 119701.
(16) Kumar, R.; Mondal, K.; Panda, P. K.; Kaushik, A.; Abolhassani, R.; Ahuja, R.; Rubahn, H.-G.; Mishra, Y. K. Core−shell nanostructures: perspectives towards drug delivery applications. *J. Mater. Chem. B* **2020**, *8*, 8992−9027.

https://doi.org/10.1021/acsomega.2c03635
ACS Omega 2023, 8, 13551−13568

(17) Kroto, H. W.; Heath, J. R.; O'Brien, S. C.; Curl, R. F.; Smalley, R. E. C60: Buckminsterfullerene. *Nature* **1985**, *318*, 162−163.
(18) Sengul, A. B.; Asmatulu, E. Toxicity of metal and metal oxide nanoparticles: a review. *Environ. Chem. Lett.* **2020**, *18*, 1659−1683.
(19) Rana, A.; Yadav, K.; Jagadevan, S. A comprehensive review on green synthesis of nature-inspired metal nanoparticles: Mechanism, application, and toxicity. *J. Cleaner Prod.* **2020**, *272*, No. 122880.
(20) Rodríguez-San-Miguel, D.; Montoro, C.; Zamora, F. Covalent organic framework nanosheets: preparation, properties and applications. *Chem. Soc. Rev.* **2020**, *49*, 2291−2302.
(21) Fan, Y.; Zhang, J.; Shen, Y.; Zheng, B.; Zhang, W.; Huo, F. Emerging porous nanosheets: From fundamental synthesis to promising applications. *Nano Res.* **2021**, *14*, 1−28.
(22) Dubey, R.; Dutta, D.; Sarkar, A.; Chattopadhyay, P. Functionalized carbon nanotubes: Synthesis, properties and applications in water purification, drug delivery, and material and biomedical sciences. *Nanoscale Adv.* **2021**, *3*, 5722−5744.
(23) Chadar, R.; Afzal, O.; Alqahtani, S. M.; Kesharwani, P. Carbon nanotubes as an emerging nanocarrier for the delivery of doxorubicin for improved chemotherapy. *Colloids Surf., B* **2021**, *208*, No. 112044.
(24) Padash, R.; Esfahani, M. R.; Rad, A. S. The computational quantum mechanical study of sulfamide drug adsorption onto X12Y12 fullerene-like nanocages: detailed DFT and QTAIM investigations. *J. Biomol. Struct. Dyn.* **2021**, *39*, 5427−5437.
(25) Al-Otaibi, J. S.; Mary, Y. S.; Mary, Y. S.; Trivedi, R.; Chakraborty, B. Theoretical investigation on the adsorption of melamine in Al12/B12-N12/P12 fullerene-like nanocages: a platform for ultrasensitive detection of melamine. *Chem. Pap.* **2022**, *76*, 225−238.
(26) Liu, Q.; Tian, J.; Liu, J.; Zhu, M.; Gao, Z.; Hu, X.; Midgley, A. C.; Wu, J.; Wang, X.; Kong, D.; et al. Modular Assembly of Tumor-Penetrating and Oligomeric Nanozyme Based on Intrinsically Self-Assembling Protein Nanocages. *Adv. Mater.* **2021**, *33*, No. 2103128.
(27) Zhang, B.; Tang, G.; He, J.; Yan, X.; Fan, K. Ferritin nanocage: a promising and designable multi-module platform for constructing dynamic nanoassembly-based drug nanocarrier. *Adv. Drug Delivery Rev.* **2021**, *176*, No. 113892.
(28) Jeon, J.-C. designing nanotechnology QCA−multiplexer using majority function-based NAND for quantum computing. *J. Supercomput.* **2021**, *77*, 1562−1578.
(29) Ayub, A.; Shoukat, A.; Tahir, M. B.; Kanwal, H.; Sagir, M.; Rafique, M.Nanostructures: A Solution to Quantum Computation and Energy Problems. In *Nanotechnology*; Springer, 2021; pp 83−107.
(30) Kim, J. M.; Lee, C.; Lee, Y.; Lee, J.; Park, S.-J.; Park, S.; Nam, J.-M. Synthesis, Assembly, Optical Properties, and Sensing Applications of Plasmonic Gap Nanostructures. *Adv. Mater.* **2021**, *33*, No. 2170360.
(31) Liu, B.; Wang, C.; Bazri, S.; Badruddin, I. A.; Orooji, Y.; Saeidi, S.; Wongwises, S.; Mahian, O. Optical properties and thermal stability evaluation of solar absorbers enhanced by nanostructured selective coating films. *Powder Technol.* **2021**, *377*, 939−957.
(32) Wang, J.; Shen, H.; Xia, Y.; Komarneni, S. Light-activated room-temperature gas sensors based on metal oxide nanostructures: A review on recent advances. *Ceram. Int.* **2021**, *47*, 7353−7368.
(33) Cao, S.; Sui, N.; Zhang, P.; Zhou, T.; Tu, J.; Zhang, T. TiO2 nanostructures with different crystal phases for sensitive acetone gas sensors. *J. Colloid Interface Sci.* **2022**, *607*, 357−366.
(34) Pooresmaeil, M.; Namazi, H. Fabrication of a smart and biocompatible brush copolymer decorated on magnetic graphene oxide hybrid nanostructure for drug delivery application. *Eur. Polym. J.* **2021**, *142*, No. 110126.
(35) Wang, T.; Liu, Y.; Wu, Q.; Lou, B.; Liu, Z. DNA nanostructures for stimuli-responsive drug delivery. *Smart Mater. Med.* **2021**, *3*, 66−84.
(36) Yuan, X.; Pan, D.; Zhou, Y.; Zhang, X.; Peng, K.; Zhao, B.; Deng, M.; He, J.; Tan, H. H.; Jagadish, C. Selective area epitaxy of III−V nanostructure arrays and networks: Growth, applications, and future directions. *Appl. Phys. Rev.* **2021**, *8*, No. 021302.
(37) Sun, L.; Cheng, C.; Wang, S.; Tang, J.; Xie, R. Wang, Bioinspired, Nanostructure-Amplified, Subcutaneous Light Harvesting to Power Implantable Biomedical Electronics. *ACS Nano* **2021**, *15*, 12475−12482.
(38) Gerling, T.; Kube, M.; Kick, B.; Dietz, H. Sequence-programmable covalent bonding of designed DNA assemblies. *Sci. Adv.* **2018**, *4*, No. eaau1157.
(39) Rezaei, A.; Morsali, A.; Bozorgmehr, M. R.; Nasrabadi, M. Quantum chemical analysis of 5-aminolevulinic acid anticancer drug delivery systems: Carbon nanotube,−COOH functionalized carbon nanotube and iron oxide nanoparticle. *J. Mol. Liq.* **2021**, *340*, No. 117182.
(40) Al-Otaibi, J. S.; Mary, Y. S.; Mary, Y. S.; Kaya, S.; Serdaroglu, G. DFT computational study of trihalogenated aniline derivative's adsorption onto graphene/fullerene/fullerene-like nanocages, X12Y12 (X= Al, B, and Y= N, P). *J. Biomol. Struct. Dyn.* **2021**, 8630−8643.
(41) Mohammadi, M. D.; Abdullah, H. Y.; Bhowmick, S.; Biskos, G. A comprehensive investigation of the intermolecular interactions between CH2N2 and X12Y12 (X = B, Al, Ga; Y = N, P, As) nanocages. *Can. J. Chem.* **2021**, *99*, 733−741.
(42) Mohammadi, M. D.; Abdullah, H. Y.; Bhowmick, S.; Biskos, G. Theoretical investigation of X12O12 (X= Be, Mg, and Ca) in sensing CH2N2: A DFT study. *Comput. Theor. Chem.* **2021**, *1198*, No. 113168.
(43) Heravi, M. R. P.; Ebadi, A. G.; Amini, I.; Mahmood, H. K.; Alsobaei, S. A.; Mohamadi, A. Quantum chemical studies of mercaptan gas detection with calcium oxide nanocluster. *J. Mol. Model.* **2021**, *27*, No. 345.
(44) Cao, Y.; Khan, A.; Mirzaei, H.; Khandoozi, S. R.; Javan, M.; Ng Kay Lup, A.; Norouzi, A.; Lemeski, E. T.; Pishnamazi, M.; Soltani, A.; Albadarin, A. B. Investigations of adsorption behavior and anti-cancer activity of curcumin on pure and platinum functionalized B12N12 nanocages. *J. Mol. Liq.* **2021**, *334*, No. 116516.
(45) Omidi, M.; Shamlouei, H. R.; Noormohammadbeigi, M. The influence of Sc doping on structural, electronic, and optical properties of Be12O12, Mg12O12 and Ca12O12 nanocages: a DFT study. *J. Mol. Model.* **2017**, *23*, No. 82.
(46) Hussain, S.; Chatha, S. A. S.; Hussain, A. I.; Hussain, R.; Mehboob, M. Y.; Mansha, N.; Shahzad, K.; Ayub, A. Theoretical Framework of Zinc-Decorated Inorganic Mg12O12 Nanoclusters for Efficient COCl2 Adsorption: A Step Forward toward the Development of COCl2 Sensing Materials. *ACS Omega* **2021**, *6*, 19435−19444.
(47) Kamel, M.; Raissi, H.; Morsali, A.; Shahabi, M. Assessment of the adsorption mechanism of Flutamide anticancer drug on the functionalized single-walled carbon nanotube surface as a drug delivery vehicle: An alternative theoretical approach based on DFT and MD. *Appl. Surf. Sci.* **2018**, *434*, 492−503.
(48) Sajid, H.; Siddique, S. A.; Ahmed, E.; Arshad, M.; Gilani, M. A.; Rauf, A.; Imran, M.; Mahmood, T. DFT outcome for comparative analysis of Be12O12, Mg12O12 and Ca12O12 nanocages toward sensing of N2O, NO2, NO, H2S, SO2 and SO3 gases. *Comput. Theor. Chem.* **2022**, *1211*, No. 113694.
(49) Vatanparast, M.; Shariatinia, Z. AlN and AlP doped graphene quantum dots as novel drug delivery systems for 5-fluorouracil drug: theoretical studies. *J. Fluorine Chem.* **2018**, *211*, 81−93.
(50) Bagheri, R.; Babazadeh, M.; Vessally, E.; Es'haghi, M.; Bekhradnia, A. Si-doped phagraphene as a drug carrier for adrucil anti-cancer drug: DFT studies. *Inorg. Chem. Commun.* **2018**, *90*, 8−14.
(51) Frisch, M. J.; Trucks, G. W.; Schlegel, H. B.; Scuseria, G. E.; Robb, M. A..; Cheeseman, J. R.; Scalmani, G.; Barone, V.; Petersson, G. A.; Nakatsuji, H.; Li, X.; Caricato, M.; Marenich, A. V.; Bloino, J.; Janesko, B. G.; Gomperts, R.; Mennucci, B.; Hratchian, H. P.; Ortiz, J. V.; Izmaylov, A. F.; Sonnenberg, J. L.; Williams-Young, D.; Ding, F.; Lipparini, F.; Egidi, F.; Goings, J..; Peng, B.; Petrone, A.; Henderson, T.; Ranasinghe, D.; Zakrzewski, V. G.; Gao, J.; Rega, N.; Zheng, G.; Liang, W.; Hada, M.; Ehara, M.; Toyota, K.; Fukuda, R.; Hasegawa, J.;

https://doi.org/10.1021/acsomega.2c03635
ACS Omega 2023, 8, 13551−13568

Ishida, M.; Nakajima, T.; Honda, Y.; Kitao, O.; Nakai, H.; Vreven, T.; Throssell, K.; Montgomery, J. A., Jr.; Peralta, J. E.; Ogliaro, F.; Bearpark, M. J.; Heyd, J. J.; Brothers, E. N.; Kudin, K. N.; Staroverov, V. N.; Keith, T. A.; Kobayashi, R.; Normand, J.; Raghavachari, K.; Rendell, A. P.; Burant, J. C.; Iyengar, S. S.; Tomasi, J.; Cossi, M.; Millam, J. M.; Klene, M.; Adamo, C.; Cammi, R.; Ochterski, J. W.; Martin, R. L.; Morokuma, K.; Farkas, O.; Foresman, J. B.; Fox, D. J.. *Gaussian 16*, Revision C.01: Wallingford, CT, 2016.

(52) Becke, A. D. A new mixing of Hartree−Fock and local density-functional theories. *J. Chem. Phys.* **1993**, *98*, 1372−1377.

(53) Mohammadi, M. D.; Abdullah, H. Y.; Biskos, G.; Bhowmick, S. Enhancing the absorption of 1-chloro-1, 2, 2, 2-tetrafluoroethane on carbon nanotubes: an ab initio study. *Bul. Mater. Sci.* **2021**, *44*, No. 198.

(54) Tomasi, J.; Mennucci, B.; Cammi, R. Quantum mechanical continuum solvation models. *Chem. Rev.* **2005**, *105*, 2999−3094.

(55) Lu, T.; Chen, F. Multiwfn: a multifunctional wavefunction analyzer. *J. Comput. Chem.* **2012**, *33*, 580−592.

(56) Adamiak, M.; Ignaczak, A. DFT studies on the physicochemical properties of a new potential drug carrier containing cellobiose units and its complex with paracetamol. *Struct. Chem.* **2022**, *33*, 1365−1378.

(57) Grimme, S. Accurate description of van der Waals complexes by density functional theory including empirical corrections. *J. Comput. Chem.* **2004**, *25*, 1463−1473.

(58) Soltani, A.; Baei, M. T.; Lemeski, E. T.; Kaveh, S.; Balakheyli, H. A DFT study of 5-fluorouracil adsorption on the pure and doped BN nanotubes. *J. Phys. Chem. Solids* **2015**, *86*, 57−64.

(59) Zhang, L.; Qi, Z.-D.; Ye, Y.-L.; Li, X.-H.; Chen, J.-H.; Sun, W.-M. DFT study on the adsorption of5-fluorouracil on B40, B39M, M@B40 (M = Mg, Al, Si, Mn, Cu, Zn). *RSC Adv.* **2021**, *11*, 39508−39517.

(60) Butt, A. R.; Ejaz, S.; Baron, J. C.; Ikram, M.; Ali, S. CaO nanoparticles as a potential drug delivery agent for biomedical applications. *Dig. J. Nanomater. Biostruct.* **2015**, *10*, 799−809.

(61) Kurban, M.; Muz, İ. Theoretical investigation of the adsorption behaviors of fluorouracil as an anticancer drug on pristine and B-, Al-, Ga-doped C36 nanotube. *J. Mol. Liq.* **2020**, *309*, No. 113209.

(62) Mohammadi, M. D.; Abdullah, H. Y. Adsorption of 1-chloro-1, 2, 2, 2-tetrafluoroethane on pristine, Al, Ga-doped boron nitride nanotubes: a study involving PBC-DFT, NBO analysis, and QTAIM. *Can. J. Chem.* **2021**, *99*, 51−62.

(63) Tu, X.; Xu, H.; Li, C.; Liu, X.; Fan, G.; Sun, W. Adsorption performance of boron nitride nanomaterials as effective drug delivery carriers for anticancer drugs based on density functional theory. *Comput. Theor. Chem.* **2021**, *1203*, No. 113360.

(64) Mohammadi, M. D.; Abdullah, H. Y.; Suvitha, A. The adsorption of 1-chloro-1, 2, 2, 2-tetrafluoroethane onto the pristine, Al-, and Ga-doped boron nitride nanosheet. *Iran. J. Sci. Technol., Trans. A: Sci.* **2021**, *45*, 1287−1300.

(65) de Oliveira, O. V.; Pires, J. M.; Neto, A. C.; dos Santos, J. D. Computational studies of the Ca12O12, Ti12O12, Fe12O12 and Zn12O12 nanocage clusters. *Chem. Phys. Lett.* **2015**, *634*, 25−28.

(66) Zhihong, Y.; Ye, Y.; Pejhan, A.; Nasr, A.; Nourbakhsh, N.; Tayebee, R. A theoretical study on the pure and doped ZnO nanoclusters as effective nanobiosensors for 5-fluorouracil anticancer drug adsorption. *Appl. Organomet. Chem.* **2020**, *34*, No. e5534.

(67) Emori, W.; Ogunwale, G. J.; Louis, H.; Agwamba, E. C.; Wei, K.; Unimuke, T. O.; Cheng, C.; Ejiofor, E. U.; Asogwa, F. C.; Adeyinka, A. S. Spectroscopic (UV−vis, FT-IR, FT-Raman, and NMR) analysis, structural benchmarking, molecular properties, and the in-silico cerebral anti-ischemic activity of 2 amino-6-ethoxybenzothiazole. *J. Mol. Struct.* **2022**, No. 133318.

(68) Cardoso, R. M.; Martins, P. A.; Ramos, C. V.; Cordeiro, M. M.; Leote, R. J.; Naqvi, K. R.; Vaz, W. L.; Moreno, M. J. Effect of dipole moment on amphiphile solubility and partition into liquid ordered and liquid disordered phases in lipid bilayers. *Biochim. Biophys. Acta, Biomembr.* **2020**, *1862*, No. 183157.

(69) Hodgkin, E. E.; Richards, W. G. Molecular similarity based on electrostatic potential and electric field. *Int. J. Quantum Chem.* **1987**, *32*, 105−110.

(70) Li, W.; Zhao, T. Hydroxyurea anticancer drug adsorption on the pristine and doped C70 fullerene as potential carriers for drug delivery. *J. Mol. Liq.* **2021**, *340*, No. 117226.

(71) Mohammadi, M. D.; Hamzehloo, M. The adsorption of bromomethane onto the exterior surface of aluminum nitride, boron nitride, carbon, and silicon carbide nanotubes: a PBC-DFT, NBO, and QTAIM study. *Comput. Theor. Chem.* **2018**, *1144*, 26−37.

(72) Glendening, E. D.; Landis, C. R.; Weinhold, F. Natural bond orbital methods. *WIRES Comput. Mol. Sci.* **2021**, *2*, 1−42.

(73) Weinhold, F. Natural Bond Orbital Analysis: A Critical Overview of its Relationship to Alternative Bonding Perspectives. *J. Comput. Chem.* **2012**, *33*, 2363−2379.

(74) Bassey, V. M.; Apebende, C. G.; Idante, P. S.; Louis, H.; Emori, W.; Cheng, C.-R.; Agwupuye, J. A.; Unimuke, T. O.; Wei, K.; Asogwa, F. C. Vibrational Characterization and Molecular Electronic Investigations of 2-acetyl-5-methylfuran using FT-IR, FT-Raman, UV−VIS, NMR, and DFT Methods. *J. Fluoresc.* **2022**, *32*, 1005−1017.

(75) Chen, X.; Sun, Z.; Zhang, H.; Onsori, S. Effect of metal atoms on the electronic properties of metal oxide nanoclusters for use in drug delivery applications: a density functional theory study. *Mol. Phys.* **2020**, *118*, No. e1692150.

(76) Enudi, O. C.; Louis, H.; Ogunwale, G. J.; Kadiri, M. T.; Okibe, P. M.; Adejoro, I. A.; Gber, T. E.; Pembere, A. M.; Adewale, A. E.Understanding the Electronic Interactions, Vertical Excitation Analysis, and the Photovoltaic Properties of 5-(2-ethylhexyl)-1, 3-di (furan-2-yl)-4H-thieno [3, 4-c] pyrrole-4, 6-dione*Res. Square*2021, DOI: 10.21203/rs.3.rs-978991/v1.

(77) Benramache, S.; Belahssen, O.; Guettaf, A.; Arif, A. Correlation between electrical conductivity—optical band gap energy and precursor molarities ultrasonic spray deposition of ZnO thin films. *J. Semicond.* **2013**, *34*, No. 113001.

(78) Ernzerhof, M. Validity of the extended Koopmans' theorem. *J. Chem. Theory Comput.* **2009**, *5*, 793−797.

(79) Islam, N.; Ghosh, D. C. The electronegativity and the global hardness are periodic properties of atoms. *J. Quantum Inf. Sci.* **2011**, *01*, 135−141.

(80) Chattaraj, P. K.; Maiti, B.; Sarkar, U. Philicity: a unified treatment of chemical reactivity and selectivity. *J. Phys. Chem. A* **2003**, *107*, 4973−4975.

(81) Unimuke, T. O.; Louis, H.; Eno, E. A.; Agwamba, E. C.; Adeyinka, A. S. Meta-Hybrid Density Functional Theory Prediction of the Reactivity, Stability, and IGM of Azepane, Oxepane, Thiepane, and Halogenated Cycloheptane. *ACS Omega* **2022**, *7*, 13704−13720.

(82) Parthasarathi, R.; Padmanabhan, J.; Elango, M.; Subramanian, V.; Chattaraj, P. Intermolecular reactivity through the generalized philicity concept. *Chem. Phys. Lett.* **2004**, *394*, 225−230.

(83) Unimuke, T. O.; Louis, H.; Emori, W.; Idante, P. S.; Agwamba, E. C.; Nwobodo, I. C.; Wei, K.; Cheng, C.-R.; Adalikwu, S. A.; Bassey, V. M.; Anyama, C. A. Spectroscopic and molecular electronic property investigation of 2-phenylpyrimidine-4, 6-diamine via 1H-NMR, UV−vis, FT-Raman, FT-IR, and DFT approach. *J. Mol. Struct.* **2022**, *1263*, No. 133195.

(84) Louis, H.; Gber, T. E.; Asogwa, F. C.; Eno, E. A.; Unimuke, T. O.; Bassey, V. M.; Ita, B. I. Understanding the lithiation mechanisms of pyrenetetrone-based carbonyl compound as cathode material for lithium-ion battery: Insight from first principle density functional theory. *Mater. Chem. Phys.* **2022**, *278*, No. 125518.

(85) Popelier, P. L. A. Quantum molecular similarity. 1. BCP space. *J. Phys. Chem. A* **1999**, *103*, 2883−2890.

(86) Matta, C. F.Hydrogen−Hydrogen Bonding: the Non-Electrostatic Limit of Closed-Shell Interaction between Two Hydro. In *Hydrogen Bonding—New Insights*; Springer: Dordrecht, 2006; Vol. 3, pp 337−375.

(87) Osigbemhe, I. G.; Louis, H.; Khan, E. M.; Etim, E. E.; Odey, D. O.; Oviawe, A. P.; Edet, H. O.; Obuye, F. Synthesis, characterization,

DFT studies, and molecular modeling of 2-(-(2-hydroxy-5-methoxyphenyl)-methylidene)-amino) nicotinic acid against some selected bacterial receptors. *J. Iran. Chem. Soc.* **2022**, *19*, 3561−3576.
(88) Bohórquez, H. J.; Boyd, R. J.; Matta, C. F. Molecular model with quantum mechanical bonding information. *J. Phys. Chem. A* **2011**, *115*, 12991−12997.
(89) Chai, J.-D.; Head-Gordon, M. Long-range corrected hybrid density functionals with damped atom−atom dispersion corrections. *Phys. Chem. Chem. Phys.* **2008**, *10*, 6615−6620.
(90) Keith, T.; Bader, R.; Aray, Y. Structural homeomorphism between the electron density and the virial field. *Int. J. Quantum Chem.* **1996**, *57*, 183−198.
(91) Onsori, S.; Alipour, E. A theoretical investigation on the adsorption of platinol drug on a ZnO nanocluster: solvent and density functional effect. *J. Mol. Liq.* **2018**, *256*, 558−564.
(92) Humphrey, W.; Dalke, A.; Schulten, K. VMD: visual molecular dynamics. *J. Mol. Graphics* **1996**, *14*, 33−38.
(93) Agobi, A. U.; Louis, H.; Ekpunobi, A.; Unimuke, T. O.; Ikeuba, A. I.; Pembere, A. M. S.; Ozoemena, C. N. Theoretical investigation of the structural, optoelectronic, and the application of waste graphene oxide/polymer nanocomposite as a photosensitizer. *Mater. Res. Express* **2022**, *9*, No. 065301.
(94) Jasim, S. A.; Maashi, M. S.; Kadhim, M. M.; Thangavelu, L.; Bashar, B. S.; Riadi, Y.; Mohamadi, A. Application of Ca12O12 nanocage for detection of aluminum phosphide molecule: First-principles investigation. *Comput. Theor. Chem.* **2022**, *1209*, No. 113615.
(95) Mohammadi, M. D.; Abdullah, H. Y. Vinyl chloride adsorption onto the surface of pristine, Al-, and Ga-doped boron nitride nanotube: A DFT study. *Solid State Commun.* **2021**, *337*, No. 114440.
(96) Kartika, R.; Alsultany, F. H.; Jalil, A. T.; Mahmoud, M. Z.; Fenjan, M. N.; Rajabzadeh, H. Ca12O12 nanocluster as highly sensitive material for the detection of hazardous mustard gas: Density-functional theory. *Inorg. Chem. Commun.* **2022**, *137*, No. 109174.
(97) Rad, A. S.; Aghaei, S. M.; Pazoki, H.; Binaeian, E.; Mirzaei, M. Surface interaction of H2O and H2S onto Ca12O12 nanocluster: Quantum-chemical analyses. *Surf. Interface Anal.* **2018**, *50*, 411−419.

https://doi.org/10.1021/acsomega.2c03635
ACS Omega 2023, 8, 13551−13568